České vysoké učení technické v Praze
Fakulta jaderná a fyzikálně inženýrská

Katedra fyziky
Program: Jaderná a částicová fyzika

Přechod elektronových svazků z vakua do plazmatu při externím vstříknutí do brázdové vlny generované laserovým impulsem

DIPLOMOVÁ PRÁCE

Vypracoval:	Bc. David Gregocki
Vedoucí práce:	Ing. Miroslav Krůs, Ph.D.
Konzultant:	Ing. Dominika Mašlárová
Rok:	2023

Czech Technical University in Prague
Faculty of Nuclear Sciences and Physical
Engineering

Department of Physics
Study programme: Nuclear and Particle Physics

Transition of electrons beams between vacuum and plasma in the external injection into a laser wakefield accelerator

MASTER THESIS

Author: Bc. David Gregocki
Supervisor: Ing. Miroslav Krůs, Ph.D.
Consultant: Ing. Dominika Mašlárová
Year: 2023

FAKULTA JADERNÁ A FYZIKÁLNĚ INŽENÝRSKÁ

KATEDRA FYZIKY

ZADÁNÍ DIPLOMOVÉ PRÁCE

Akademický rok: 2022/2023

ČVUT

ČESKÉ VYSOKÉ
UČENÍ TECHNICKÉ
V PRAZE

Student:	Bc. David Gregocki
Studijní program:	Jaderná a částicová fyzika
Název práce: *(česky)*	Přechod elektronových svazků z vakua do plazmatu při externím vstříknutí do brázdové vlny generované laserovým impulsem
Název práce: *(anglicky)*	Transition of electrons beams between vacuum and plasma in the external injection into a laser wakefield accelerator
Jazyk práce:	Angličtina

Pokyny pro vypracování:

1) Popište metodu urychlování elektronů brázdovou vlnou pomocí laseru (angl. „laser wakefield acceleration").

2) Popište princip externího vstříknutí elektronů do brázdové vlny. Speciálně se zaměřte na přechod elektronového svazku mezi vakuem a plazmatem.

3) Seznamte se s metodou kinetického numerického modelování "particle-in-cell" (PIC). Seznamte se s prostředím výpočetního gridu MetaCentrum a vzdáleným zpracováním a vyhodnocováním dat z PIC kódu.

4) Pomocí vhodně zvoleného PIC kódu prostudujte efektivitu záchytu elektronového svazku při přechodu mezi vakuem a plazmatem a navrhněte způsob, jak by se efektivita dala vylepšit.

Doporučená literatura:

[1] Esarey, E., Schroeder, C. B., a Leemans, W.P. Physics of laser-driven plasma-based electron accelerators. Reviews of Modern Physics 81.3 (2009): 1229.

[2] Marchetti, B., et al. Conceptual and technical design aspects of accelerators for external injection in LWFA. Applied Sciences 8.5 (2018): 757.

[3] Svystun, E. N., et al. Two-stage laser-driven plasma acceleration with external injection for EuPRAXIA. Journal of Physics: Conference Series 1067 (2018): 4.

[4] Derouillat, J., et al. Smilei: A collaborative, open-source, multi-purpose particle-in-cell code for plasma simulation. Computer Physics Communications 222 (2018): 351-373.

Jméno a pracoviště vedoucího diplomové práce:

Ing. Miroslav Krůs, Ph.D.
Ústav fyziky plazmatu Akademie věd ČR, v. v. i.
Katedra fyziky, Fakulta jaderná a fyzikálně inženýrská, ČVUT v Praze
Jméno a pracoviště konzultanta:
Ing. Dominika Mašlárová
Ústav fyziky plazmatu Akademie věd ČR, v. v. i.
Katedra fyzikální elektroniky, Fakulta jaderná a fyzikálně inženýrská, ČVUT v Praze
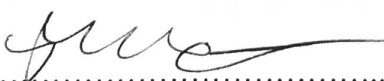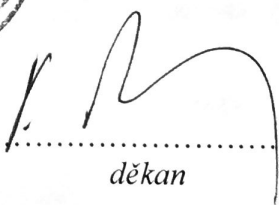
Datum zadání diplomové práce:　　　20.10.2022

Termín odevzdání diplomové práce:　03.05.2023

Doba platnosti zadání je dva roky od data zadání.

....
garant studijního programu

....
vedoucí katedry

....
děkan

V Praze dne　20.10.2022

ČESKÉ VYSOKÉ UČENÍ TECHNICKÉ V PRAZE
Fakulta jaderná a fyzikálně inženýrská

Břehová 7
115 19 Praha 1

P R O H L Á Š E N Í

Já, níže podepsaný

Jméno a příjmení studenta:	David Gregocki
Osobní číslo:	473403
Název studijního programu (oboru):	Jaderná a částicová fyzika

prohlašuji, že jsem diplomovou práci s názvem:

Přechod elektronových svazků z vakua do plazmatu při externím vstříknutí do brázdové vlny generované laserovým impulsem

vypracoval samostatně a uvedl veškeré použité informační zdroje v souladu s Metodickým pokynem o dodržování etických principů při přípravě vysokoškolských závěrečných prací.

V Praze dne 3.5.2023

..............*Gregocki*..............
podpis

Acknowledgement

Bc. David Gregocki

Abstrakt: Urýchľovanie brázdovou vlnou je efektívna metóda zrýchlenia elektrónov v plazme, ktorá umožňuje generovať vysoké gradienty elektrického poľa. Tradičné schémy vstrekovania elektrónov do brázdovej vlny však môžu často trpieť nedostatočnou kontrolou. Preto rastie záujem o skúmanie externého vstrekovania, pri ktorom sa zväzky elektrónov vstrekujú z externého urýchľovača. Prudký prechod z vákua do plazmy avšak môže zapríčiniť zhoršenie parametrov elektrónového zväzku. Z toho dôvodu sa v rámci tejto práce uskutočnili 2D a 3D particle-in-cell simulácie pomocou kódu Smilei. Konkrétne boli analyzované (desiatky mikrónov dlhé) hustotné nábehy plazmy rôznych dĺžok s lineárnym alebo parabolickým nárastom, aby sa určil ich vplyv na vstrekovanie elektrónového zväzku a vývoj jeho parametrov v čase. S daným súborom parametrov simulácie bol navrhnutý 400-µm hustotný nábeh plazmy konvexného parabolického profilu ako najefektívnejší pri zachovaní relatívneho energetického rozptylu a priečnej emitancie elektrónového zväzku.
Kľúčová slova: urýchľovanie brázdovou vlnou, bublinový režim, externé vstrekovanie, particle-in-cell simulácie, lineárne a parabolické hustotné nábehy plazmy

Abstract: Laser wakefield acceleration is an efficient method for electron acceleration in plasmas that ensures high electric field gradients. However, traditional injection schemes of electrons into the wakefield can often suffer from a lack of control. Consequently, there is a growing interest in investigating external injection, in which electron bunches are injected from a separate accelerator. Nevertheless, a sharp vacuum-plasma transition can cause deterioration of the bunch parameters. Therefore, in this work, 2D and 3D particle-in-cell simulations using the Smilei code were performed. Short (tens-of-micron scale) plasma density ramps of different lengths with a linear or parabolic increase were examined to determine their influence on the injection of the electron bunch and its parameters. With a given set of simulation parameters, the 400-µm plasma density ramp of a convex parabolic profile was suggested as the most effective one in preserving the relative energy spread and transverse emittance of the electron bunch.
Key words: laser wakefield acceleration, bubble regime, external injection, particle-in-cell simulations, linear and parabolic plasma density ramps

Contents

Introduction

Laser wakefield acceleration (LWFA) is a promising technique of the electron acceleration in the field of electron accelerator technology dedicated to high-energy particle physics. It involves the interaction of an intense laser pulse with plasma, which creates a high-amplitude electric field capable of accelerating electrons to relativistic speeds. Moreover, it has several advantages compared to traditional acceleration techniques, such as radio-frequency accelerators. It can accelerate particles to high energies over a much shorter distance, reducing the cost and complexity of the particle accelerator. Additionally, electron beams produced by laser wakefield acceleration are highly focused and collimated. Such beams can be used in a range of applications, such as advanced medical imaging [1], the study of ultra-fast dynamics in solids, molecules, or chemical reactions [2].

However, experiments demonstrating laser wakefield acceleration with the use of the highly non-linear regime often suffer from shot-to-shot fluctuations or a lack of control over the electron bunch parameters. This is partly because these experiments use plasma as a source of electron beams and, at the same time, as an accelerating medium. Particularly, as an intense laser creates a non-linear wakefield, while the surrounding plasma electrons are accumulated in the rear part of the first bubble, some of them are subsequently injected into the accelerating structure. Such an injection process, however, can cause that injected electrons acquire undesirable properties (increased emittance, energy spread or divergence) even before they are subjected to acceleration. Generally, it is desirable to obtain electron beams with minimal divergence or energy spread so that following beam optics are not burdened by extreme requirements and the emittance growth is as small as possible [3].

On the other hand, injection of the electron bunch produced by an external source, i.e., external injection [4], can represent an effective method for producing stable and high-quality electron beams, as it takes advantage of the fact that these electrons have well-known and, in this sense, "fixed" initial parameters. Therefore, this technique has generated much interest in the scientific community. It should be noted that external injection is experimentally more demanding than traditional LWFA injection schemes as it requires exquisite alignment and timing between the electron bunch and the laser. It also requires vacuum isolation between the conventional RF accelerator and the LWFA stage.

In most cases, only sharp vacuum-plasma transitions are studied, and it has been demonstrated that such options can cause a rapid emittance growth [5]. In order to solve this issue, it has been demonstrated that by adding smooth, long (mm-scale) density ramps, it is possible to mitigate the emittance growth [6].

The purpose of this work is to examine and determine if also short (tens-of-micron scale) plasma density ramps of different lengths and profiles play a significant role in the injection of the electron bunch and its parameters. Particularly, eight different lengths (varying from 25 to 700 µm) of plasma ramps, both linear and convex parabolic (as typical density profiles), were considered. In order to determine their effect on the electron bunch, 2D and also 3D particle-in-cell simulations using the Smilei code [7] were performed.

This work is organized in the following way: The first chapter includes a brief introduction to plasma acceleration. Basic aspects of laser and plasma physics are also mentioned. At the end of the first chapter, the two main regimes of laser wakefield acceleration are described, along with its limitations. The second chapter deals with the external injection of the electron bunch into the wakefield. The phenomena that are accompanied by this process and can affect the quality of the electron bunch are also outlined. In order for such a description to be complete, several options for maintaining the quality of the bunch during the injection and subsequent acceleration were mentioned. The third chapter includes a brief history and basic knowledge about particle-in-cell simulations, along with numerical instabilities that can affect their results. The last, fourth, chapter is dedicated to the results obtained from 2D and 3D simulations. Electron bunch parameters that were investigated either in the given positions or in the entire time range of the simulation were mean energy, energy spread, relative energy spread, and transverse emittance. Based on this, the most effective parameters were suggested.

Chapter 1

Laser wakefield acceleration (LWFA)

1.1 Plasma accelerators

Conventional accelerators use electrostatic, pulsed, or radio-frequency electromagnetic fields to accelerate charged particles in a vacuum. In such a manner, depending on the application, various particles with different charges are accelerated to desired kinetic energy up to TeV range [8]. Unfortunately, the acceleration field of this technology is constrained by an upper limit of around 100 MV/m [9], [10]. Beyond this, the acceleration field becomes unfeasible due to the vacuum breakdown of the accelerator cavity walls, which will destroy the cavity itself. In practical usage, however, conventional accelerators operate with an acceleration gradient of typically ~ 10 MV/m [9], [10].

The highest energy in the world is currently reached by the circular collider LHC at CERN (13.6 TeV collision energy), which has a radius ~ 27 km. To obtain higher acceleration energies while using the conventional method without damaging the accelerating structure would mean the construction of even larger circular accelerators, which is financially and technologically demanding.

Another way to overcome mentioned acceleration field's upper limit of conventional accelerators is to use local electric fields that can be generated inside plasma. Plasma is not limited by electrical breakdowns and, thus, an accelerating gradients up to 200 GV/m can be achieved [10], [11]. Therefore, plasma accelerators could represent a compact alternative to conventional accelerators, which would also reduce the cost of their construction. At the same time, plasma accelerators can produce electron beams with properties suitable for new applications. Moreover, plasma accelerators can obtain ultra-short electron beams with the duration in the order of femtoseconds without requiring complicated compression schemes. This feature can be used in the study of fast dynamics in solids, molecules, or chemical reactions, and, together with the undulators in a tunable, table-top X-ray laser [12], [13].

Currently, there are several methods of plasma acceleration. One of the most researched methods based on the use of a high-intensity laser is laser wakefield acceleration (LWFA). Lasers that produce an ultra-short, high-intensity pulse are specially designed so that the acceleration of charged particles by the laser pulse takes place in a plasma (with a density of 10^{16} cm^{-3} $< n_e <$ 10^{19} cm^{-3}), which provides an environment to generate a plasma wave suitable for the acceleration (wakefield). Typical wavelengths are in the order of $\lambda_p \sim$ 10 - 100 μm.

In order to better understand how the plasma wakefield is generated by the laser pulse, it is useful to point out how light and waves propagate in cold plasma.

1.2   Wave propagation in cold plasmas

The analysis of plasma waves is interesting by itself since it reveals how electrons, ions, and electromagnetic fields react differently to small perturbations or the same frequency. In general, the cold plasma equations describe waves which propagate through plasma much faster than a typical thermal velocity. Moreover, equations representing the propagation of waves are greatly simplified when the cold plasma model is applied. Given that the particles are initially at rest in the cold plasma model, they have no kinetic thermal motion of their own. The cold plasma model can still be used for laser wakefield acceleration because the phase velocity of the excited waves (which is approximately the speed of light c) is much larger than the thermal velocity of the electrons ($|v_{th}| \sim 1.3 \cdot 10^6$ m/s).

For this treatment, we will regard the plasma as a cold collisionless fluid. Generally, plasma can be defined as a "quasi-neutral gas of charged and neutral particles which exhibits collective behaviour" [14]. In that context, electrons are treated as a fluid with the ions treated as a fixed neutral background. The dynamics of charged particles is described by the Maxwell equations.

$$\nabla \times \mathbf{E} = -\frac{\partial \mathbf{B}}{\partial t}, \tag{1.1}$$

$$\nabla \times \mathbf{B} = \mu_0 \left(\mathbf{J} + \varepsilon_0 \frac{\partial \mathbf{E}}{\partial t} \right), \tag{1.2}$$

where $\mathbf{E}$ is the electric field, $\mathbf{B}$ is a magnetic field, and $\mathbf{J}$ is an electric current, μ_0 and ε_0 are vacuum permeability and permittivity, respectively, and t is time. These equations can be transformed to the wave equation by taking the curl of (1.1) and substituting it into (1.2)

$$\nabla^2 \mathbf{E} - \nabla \left(\nabla \cdot \mathbf{E} \right) = \mu_0 \frac{\partial \mathbf{J}}{\partial t} + \mu_0 \varepsilon_0 \frac{\partial^2 \mathbf{E}}{\partial t^2}. \tag{1.3}$$

Furthermore, the single-particle model for cold plasmas can be applied. In the linear case ($|v_e|/c \ll 1$) the response of an electron of mass m_e and charge $-e$ to an electric field $\mathbf{E}(t)$ is described by the Newton's second law

$$m_e \frac{\partial \mathbf{v_e}}{\partial t} = -e\mathbf{E}, \tag{1.4}$$

with the velocity of the electron $\mathbf{v_e}$. If the ions are treated indeed as stationary, the current density comes approximately entirely from the electron motion

$$\mathbf{J} = -en_e\mathbf{v_e}, \tag{1.5}$$

where n_e is electron density. To obtain the source term in (1.3), one can take the time derivative of this equation and substitute (1.4) to get

$$\frac{\partial \mathbf{J}}{\partial t} = \mu_0\varepsilon_0 \frac{n_e e^2}{\varepsilon_0 m_e}. \tag{1.6}$$

By substituting (1.6) in (1.3), the wave equation for waves in a cold plasma can be written as

$$\nabla^2\mathbf{E} - \nabla\left(\nabla\cdot\mathbf{E}\right) = \frac{1}{c^2}\frac{n_e e^2}{\varepsilon_0 m_e}\mathbf{E} + \frac{1}{c^2}\frac{\partial^2\mathbf{E}}{\partial t^2}, \tag{1.7}$$

for $c = 1/\sqrt{\mu_0\varepsilon_0}$. This is important result from which the frequency of plasma waves (which is crucial for laser wakefield acceleration) together with dispersion relation can be derived.

1.3 Plasma frequency

The term quasi-neutral, which was mentioned in the previous section, implies that the overall charge of plasma is approximately neutral. This requires the system to have a large enough spatial extent such that local perturbations of the charge density do not affect the overall neutrality. These local charge imbalances can be created by pulling a bunch of electrons away from their equilibrium position, thus resulting in the generation of the electric field. Consequently, this electric field tries to attract the electrons back to their initial equilibrium position. Due to their inertia, however, the electrons will repeatedly overshoot this position, which results in simple harmonic oscillations. Given that the ions are much heavier than the electrons, ions will remain almost at the initial position, so they can be considered as stationary. Therefore, the formed density modulations, referred to as plasma oscillations, are characterized by a frequency of oscillations called electron plasma frequency. In this section and the following chapters, the term plasma frequency will be exclusively used for the plasma electron frequency.

The periodic electric field that pushes electrons back to their neutral positions can be written as

$$\mathbf{E} = E_0 \exp[i(kz - \omega t)]\tilde{\mathbf{z}}, \tag{1.8}$$

where E_0 is the amplitude, k is the wavenumber, ω is the angular frequency, and $\tilde{\mathbf{z}}$ is the direction of electron movement. Using (1.7), we obtain

$$\left(\frac{n_e e^2}{\varepsilon_0 m_e c^2} - \frac{\omega^2}{c^2}\right)E_z = 0, \tag{1.9}$$

for the electric field perturbation in the z direction E_z, which leads to the dispersion relation for plasma oscillations (i.e., Langmuir waves)

$$\omega = \omega_p, \tag{1.10}$$

where

$$\omega_p = \sqrt{\frac{n_e e^2}{\varepsilon_0 m_e}}, \tag{1.11}$$

is the plasma frequency [15].

It should be noted the dispersion relation in (1.10) is only valid in the 1D case of neutral cold plasma, assuming the electric field $\mathbf{E}$ is predominantly parallel to the motion of the plasma electrons. Although this relation holds in the non-linear limit and Langmuir with Tonks were able to derive the plasma frequency from it [15], in any practical system, there will always be variation in the transverse direction. This correction would lead to the dispersion relation that will be derived in the following section.

1.4   Propagation of light in plasma

In general, electromagnetic waves are transverse. This characteristic can be conveniently used to calculate the propagation of light through a plasma, as the wave equation derived in Section 1.2 can be recast as

$$\nabla^2 \mathbf{E} = \frac{\omega_p^2}{c^2}\mathbf{E} + \frac{1}{c^2}\frac{\partial^2 \mathbf{E}}{\partial t^2}. \tag{1.12}$$

For the electromagnetic wave propagating in the z direction and polarized in the x direction, the electric field with amplitude E_0 can be written as

$$\mathbf{E} = E_0 \exp i(k_L z - \omega_L t)\tilde{\mathbf{x}}, \tag{1.13}$$

where ω_L is the wave frequency and k_L is the wavenumber. Substituting this to (1.12) leads to the dispersion relation

$$\omega^2 = \omega_p^2 + k_L^2 c^2, \tag{1.14}$$

which includes the wavenumber of the electromagnetic wave k_L and plasma frequency ω_p derived in (1.11).

1.5   High-intensity, ultra-short Gaussian laser beams

One of the most significant milestones in laser physics and technology over the last decade has been the development of lasers capable of generating ultra-short $>$ TW pulses without damaging the gain media. In general, high-intensity lasers work in different modes. Nowadays, they can reach a maximum power up to 10^{16} W and generate pulses with durations of 10^{-10}-10^{-15} s, intensities up to 10^{23} W·cm^{-2} [16] and repetition rates in the range of 10^3-10^6 Hz. Such properties enable the investigation of new phenomena within their interaction with atoms and molecules. Moreover, these lasers are used in state-of-the-art research and have many potential applications [2].

To obtain highly intense laser fields, a concentration of large amounts of radiation energy within very short time intervals is required while the laser beam is focused on a small area [17]. These requirements can be fulfilled using mode-locking [18] and chirped pulse amplification (CPA) [19].

CPA is a very effective method of laser pulse energy amplification, which was invented in 1985 by D. Strickland and G. Mourou [19]. The basis lies in the generation of short laser pulses in a laser oscillator via mode-locking, which are then spectrally and temporally stretched, and introduced to a conventional laser amplification chain. Each laser pulse is subsequently compressed back, ideally to its initial duration and direction, and later focused if needed. The development of CPA has revolutionized laser physics by allowing the generation of ultra-short (fs- to ps-scale) high-intensity laser pulses with the aforementioned properties, which are necessary in order to drive plasma waves to accelerate particles.

In such high-intensity laser systems and also in laser-plasma acceleration, high-intensity laser pulses can be described in a simplified way as a monochromatic plane wave modulated by a Gaussian envelope[1] [21]. Assuming polarization in the x axis and propagation in the z axis, the electric field is given by

$$\mathbf{E}(r, z) = E_0 \hat{\mathbf{x}} \frac{w_0}{w(z)} \exp\left(\frac{-r^2}{w(z)^2}\right) \exp\left(-i\left(k_L z + k_L \frac{r^2}{2R(z)} - \psi_g(z)\right)\right), \quad (1.15)$$

where E_0 is the electric field amplitude, $w(z)$ is the radius at which the field amplitudes fall to $1/e$ of their axial values at the plane z along the beam, w_0 is the waist (the value of $w(z)$ at the focal plane), r is the radial distance from the center axis of the beam, z is the axial distance from the beam's waist, $R(z)$ is the radius of curvature of the beam's wavefronts, $\psi_g(z)$ is the Gouy phase, and $\hat{\mathbf{x}}$ is the unit vector in the x direction.

It is evident from the equation above that the propagation of the Gaussian laser pulse is characterized by $w(z)$, $R(z)$, $\psi_g(z)$. As illustrated in Figure 1.1, these parameters evolve along the z axis as

$$w(z) = w_0\sqrt{1 + \left(\frac{z}{z_{\mathrm{R}}}\right)^2}, \quad R(z) = z\left[1 + \left(\frac{z_{\mathrm{R}}}{z}\right)^2\right], \quad \psi(z) = \arctan\left(\frac{z}{z_{\mathrm{R}}}\right), \quad (1.16)$$

where z represents a distance to the focal position, in which $w(z) = w_0$, and

$$z_{\mathrm{R}} = \frac{\pi w_0^2}{\lambda} \quad (1.17)$$

is called the Rayleigh length. The Rayleigh length is an important parameter that represents the distance at which the laser beam transverse area is doubled, compared with the one in the focal plane, due to diffraction. It is also related to the confocal parameter b, which is double the Rayleigh length and is often used as an estimate of the distance to which the Gaussian beam is approximately collimated [22]. Equation (1.15) is valid if $\omega_0 \geq 2\pi/\lambda_L$, where λ_L is laser beam wavelength.

---

[1]Gaussian-like laser pulse amplitude envelope is generally desirable for high energy concentration [20].
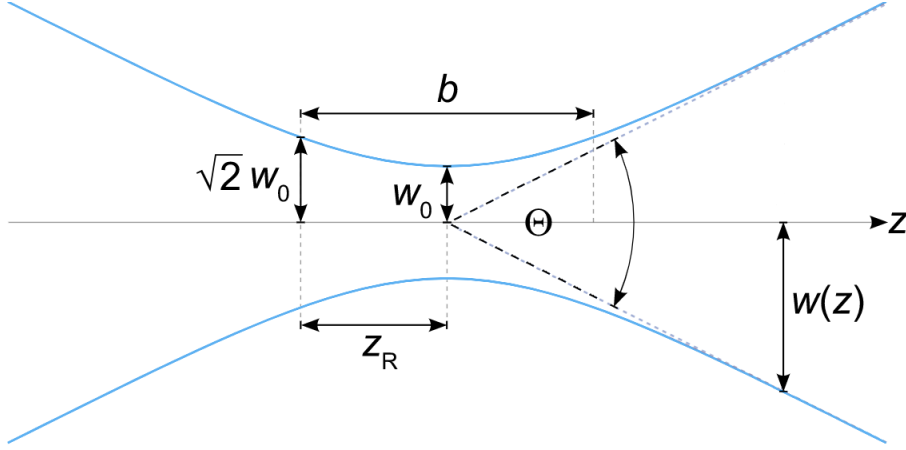
Figure 1.1: Gaussian beam width $w(z)$ as a function of the distance z along the beam where w_0 is beam waist, b is depth of focus, z_R is Rayleigh length, and θ is total angular spread.

The corresponding intensity distribution of a Gaussian laser beam is given by

$$I(r, z) = \frac{\varepsilon_0 c}{2}|E(r, z)|^2 = I_0 \left(\frac{w_0}{w(z)}\right)^2 \exp\left(\frac{-2r^2}{w(z)^2}\right). \tag{1.18}$$

The total power of the beam is $P_0 = \pi w_0^2 I_0/2$, where I_0 is the intensity at the center of the beam at its waist.

1.6   Normalized vector potential

Considering a laser pulse as a monochromatic electromagnetic wave in the vacuum, the corresponding electromagnetic fields $\mathbf{E}$ and $\mathbf{B}$ can be expressed in terms of the scalar potential Φ and the vector potential $\mathbf{A}$ as

$$\mathbf{E} = -\nabla\Phi - \frac{\partial\mathbf{A}}{\partial t};$$
$$\mathbf{B} = \nabla \times \mathbf{A}, \tag{1.19}$$

with the Coulomb gauge $\nabla \cdot \mathbf{A} = 0$.

For high power laser systems, it is convenient and common to use the normalized electrostatic and vector potentials to express the importance of relativistic effects that occur in plasma. The reason is because they have an influence on electron mass growth, which lowers the plasma frequency. These dimensionless quantities are defined as

$$\phi = \frac{e\Phi}{m_e c^2}, \qquad \mathbf{a} = \frac{e\mathbf{A}}{m_e c^2}, \tag{1.20}$$

for Φ and $\mathbf{A}$, respectively. However, in vacuum, $\Phi = 0$. In this regard, both fields, $\mathbf{E}$ and $\mathbf{B}$, depend only on the vector potential $\mathbf{A}$. Expression for $\mathbf{a}$ can be viewed as the normalized quiver momentum of the electrons in an electric field [23]. It is useful to define a laser strength parameter a_0, representing the peak amplitude of the normalized vector potential, as

$$a_0 = \frac{eA_0}{m_e c^2} = \frac{eE_0}{m_e \omega_L c}. \tag{1.21}$$

Moreover, assuming a linearly polarized laser beam with a Gaussian radial profile, peak laser intensity I_0 can be recast in relation to a_0 as

$$I_0 = \frac{c}{2\varepsilon_0} \left(\frac{m_e \pi c^2 a_0}{e \lambda_L} \right)^2, \tag{1.22}$$

which leads to

$$a_0 = \sqrt{\frac{e^2}{2\pi^2 \varepsilon_0 m_e^2 c^5} \lambda_L^2 I_0} \simeq 8.6 \cdot 10^{-10} \lambda_L [\mu\text{m}] \sqrt{I_0 [\text{W/cm}^2]}. \tag{1.23}$$

Consequently, a_0 can be effectively considered as the maximum field strength of the laser pulse at focus, given by a specific laser system. Based on a_0, it is also possible to divide LWFA into two main regimes [24], which will be described further in this chapter. In particular, if

$$\begin{aligned} a_0 \ll 1 \qquad &\Rightarrow \qquad \text{Linear regime} \\ a_0 \gg 1 \qquad &\Rightarrow \qquad \text{Bubble regime.} \end{aligned} \tag{1.24}$$

1.7 Debye shielding

Among the fundamental properties of plasma that have not been mentioned yet is the ability to shield any internal electric potentials [25]. When a charged particle is inserted into the plasma, plasma particles with the opposite charge are attracted. Meanwhile, particles with the same charge are repelled. This local charge distribution change results in the creation of a dense charged layer around each inserted particle or applied potential. Their influence on neighbouring particles in cold plasmas is thus effectively isolated within the "Debye sphere". The particular distance over which Debye shielding is applied for the plasma electrons is denoted as Debye length λ_D, defined as

$$\lambda_{\text{D}} = \sqrt{\frac{\varepsilon_0 k_{\text{B}} T_e}{n_e e^2}}, \tag{1.25}$$

where k_B is the Boltzmann constant, T_e is the temperature of plasma electrons, and e is the elementary charge. Debye length for ions would be derived analogically.

In ideal plasma, two following conditions needs to be fulfilled. The first condition is that the spatial scale of the plasma L should be much larger than its Debye length, i.e., $L \gg \lambda_D$. The second condition is related to the average number of electrons contained in a Debye sphere known as the plasma parameter, defined as

$$\Lambda = \frac{4\pi}{3} n_e \lambda_D^3, \tag{1.26}$$

that must satisfy $\Lambda \gg 1$. On this matter, the following simplification can be made. Since the collective electrostatic interactions dominate over particle-particle collisions, they can be neglected. This effectively means that the plasma particles can be investigated as if they only interact with an undisturbed background field.

It is important to note that, in plasmas with finite temperatures, Debye shielding (due to thermal motions) is not perfect and electric fields of inserted particles can be present outside the shielding layer. However, the plasmas used for plasma wakefield acceleration can still be treated as ideal [14].

1.8   Principle of laser wakefield acceleration

Laser wakefield acceleration (LWFA) has recently been considered as one of the most promising methods of acceleration of electron bunch by lasers in plasma. This status was confirmed in 2004, owing to the publications of experimental results from three independent scientific groups in the Laboratoire d'Optique Appliquée [26], Lawrence Berkeley National Laboratory [27], and Imperial College [28]. With a specific choice of laser and plasma parameters, all groups managed to generate quasi-monoenergetic electron beams with a mean energy of 100 MeV and a relative energy spread of only a few %.

The original concept of a plasma accelerator driven by an ultra-short intense laser pulse was proposed in 1979 by the physicists Tajima and Dawson [11]. At that time, it was already known that the combination of Maxwell's equations for a charged particle and an electromagnetic wave in a vacuum leads to a dispersion relation in a plasma with a frequency (1.14), where plasma frequency ω_p is given by the relation (1.11). An electromagnetic wave can propagate to plasma if its density is lower than the critical density

$$n_c = \frac{\varepsilon_0 m_e \omega_L^2}{e^2}. \tag{1.27}$$

From relation (1.11), it can be seen that ω_p is inversely proportional to mass. Thus, in the case of ions, their value is several times lower in comparison to electrons. Therefore, indeed, within LWFA and electromagnetic interactions, only the plasma frequency caused by electron motions is considered. Further in their publication, Tajima and Dawson calculated that damped harmonic oscillations can only be observed if $\omega_p \gg \nu_e$, where ν_e is the collision frequency of electrons with neutral particles. Otherwise, no periodic character is observed in changes in the electron concentration. In the case of the plasma electrons with velocities v_e, near the speed of light, relativistic effects, i.e., Lorentz factor γ and its impact on ω_p must be assumed. The Lorentz factor is defined as

$$\gamma = \frac{1}{\sqrt{1 - \frac{v_e^2}{c^2}}}. \tag{1.28}$$

In general, in a plasma-based accelerator, plasma acts as an energy transformer, where energy is transferred from an exciter (a high-energy charged beam or an ultra-short laser pulse) to the accelerated particles. As mentioned in Section 1.1, this acceleration method can achieve an accelerating gradients up to 200 GV/m. It should be noted that the plasma density ultimately limits the highest achievable value of the accelerating gradient. Because, as previously mentioned, in overdense plasma, the acceleration effectivity rapidly decreases.

The basic principle of the LWFA consists of applying an ultra-short and intense laser pulse to an underdense plasma. This idea utilizes another important property of laser pulses, which is their ability to exert a net force over charged particles. Due to the fact that the amplitude of the laser pulse intensity is generally not uniform in space but gradually changes in time, electrons will also be affected by a non-linear force proportional to the gradient of the laser intensity, called the ponderomotive force $\mathbf{F}_{pon}$, which causes the electrons to oscillate in the direction of $\mathbf{E}$.

It can be written as [29]

$$\mathbf{F}_{\text{pon}} = -\frac{\omega_{\text{p}}^2}{\omega^2} \nabla \frac{\varepsilon_0 \langle \mathbf{E}^2 \rangle}{2} = \frac{m_e c^2 a_0}{\omega_0}, \tag{1.29}$$

where $\langle \mathbf{E}^2 \rangle$ is averaged laser electric field. The last term in the relation (1.29) is valid in the relativistic case ($a_0 > 1$). Ponderomotive force can be in principle, associated with the radiation pressure of light in plasma [30].

$\mathbf{F}_{\text{pon}}$ pushes out plasma electrons in both radial and axial directions. Plasma ions are also affected, but they are too massive to move significantly under the influence of the ponderomotive force [31]. However, due to the Coulomb force, the repelled electrons are promptly attracted back to the ions and repelled again by $\mathbf{F}_{\text{pon}}$, creating another region with a lower electron concentration. These density modulations form longitudinal electric fields between regions with higher and lower electron densities [32]. The overall effects of the ponderomotive force and the movements of electrons in plasma with the frequency ω_p lead to the formation of plasma waves (wakefield).

Tajima and Dawson derived that for the formation of waves in the plasma, the relation for the electron density n_e must hold

$$n_e[\text{cm}^{-3}] \sim \frac{1.6 \cdot 10^{21}}{\tau_l^2[\text{fs}]}, \tag{1.30}$$

where τ_l is length of the laser pulse. At the time of now famous publication, obtaining femtosecond laser beams with high intensity was not achievable. Moreover, even the method of their production, such as the previously mentioned CPA [19], was not known. Therefore, the full potential of LWFA could not be utilized during that period of time. Instead, other methods of plasma acceleration were considered with more interest. [11]. As technology advanced, this was no longer an obstacle. In addition, regimes of the LWFA were described, depending on the laser intensity. Linear and non-linear regimes will be described in the next sections.

1.9 Linear regime of the LWFA

In general, the linear regime of laser wakefield acceleration can be characterized by the condition for the normalized vector potential, which is $a_0^2 \ll 1$. Such a laser pulse is able to create relatively small plasma density modulations. The mathematical description of the wakefield is straightforward. The equation for the electric field of the wave can be derived from the linearized electron fluid equations, i.e., Poisson's equation, the continuity equation, and the momentum equation. Particularly for laser-driven accelerators, this description can be given as [10]

$$\left(\frac{\partial^2}{\partial t^2} + \omega_p^2 \right) \frac{\delta n}{n_e} = c^2 \nabla^2 \frac{a^2}{2}, \tag{1.31}$$

where $\delta n / n_e \ll 1$ is the perturbed density of the plasma wave, n_e is (electron) plasma density, and $a^2 \ll 1$ is the normalized intensity of the laser pulse.

The solution to this equation is given by integrating (1.31) over time:

$$\frac{\delta n}{n_e} = \frac{c^2}{\omega_p} \int_0^t dt' \sin \omega_p \left(t - t'\right) \nabla^2 \frac{a^2}{2}. \tag{1.32}$$

Equation (1.31) can be interpreted as a forced oscillator type of equation with the ponderomotive force $\nabla^2 a^2/2$ as the driving force and the plasma response to space charge effects $\omega_p^2 \delta n/n_e$ as the restoring force. Moreover, (1.31) implies that the electric field of the wakefield can be described as

$$\mathbf{E}(\mathbf{r}, t) = -\frac{m_e c^2 \omega_p}{e} \int_0^t dt' \sin \omega_p \left(t - t'\right) \nabla \frac{a^2(\mathbf{r}, t')}{2}, \tag{1.33}$$

if $E \ll E_{l,0}$ [23] where

$$E_{l,0} = \frac{m_e c \omega_p}{e}, \tag{1.34}$$

is a longitudinal electric field responsible for the acceleration.

It is evident that the plasma wakefield (for $a_0^2 \ll 1$) has a sinusoidal shape. This can also be seen in Figure 1.2. As a result, approximately equal phase amplitudes for acceleration within each period are provided. Furthermore, considering the axial symmetry of the laser pulse, solutions to (1.32) indicate that the plasma wakefield will be generated most efficiently when the laser pulse length L is in the order of the plasma wavelength λ_p, i.e., $L \simeq \lambda_p$ [10].
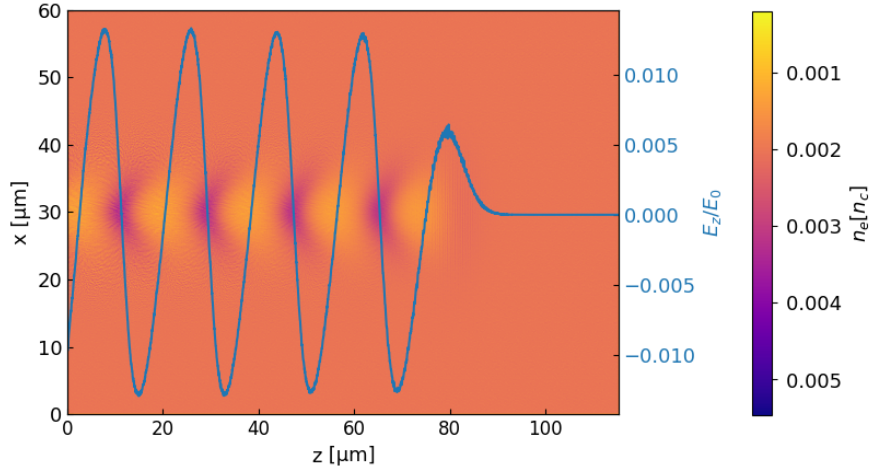
Figure 1.2: Example of the linear regime in LWFA. Plasma (electron) density profile n_e was obtained from a 2D particle-in-cell simulation using the Smilei code and $a_0 = 1.0$ (which is generally considered as an upper limit for the linear regime). Normalized wakefield values E_z/E_0 (blue line) are depicted for $x = 30$ μm.

For one dimensional case and a Gaussian profile laser pulse with $a_0^2 \ll 1$, a solution for the amplitude of the plasma wakefield can be written as [33]

$$\frac{E_{\max}}{E_{l,0}} = \left(\sqrt{\pi} \frac{a_0^2}{2}\right) k_p L \exp\left(-\frac{k_p^2 L^2}{4}\right), \tag{1.35}$$

In this regard, a maximum of the plasma wave amplitude can be observed at $k_p L = \sqrt{2}$. Substituting this value back to (1.35), one can obtain

$$E_{\max} \simeq 0.76 a_0^2 E_{l,0}. \tag{1.36}$$

1.10 Bubble regime of the LWFA

In the case when $a_0^2 \gg 1$ and the length of the driver pulse is $L \sim \lambda_p/2$, almost all plasma electrons are repelled from the region around the pulse propagation axis [23]. The laser pulse leaves behind such electron-free bubbles, this particular regime is often referred to as the bubble regime (or blowout regime). The positive charge from the ions in the region of charge separation creates a huge gradient between the back of the first bubble, where a large number of electrons are concentrated, and its interior, which predominantly consists of plasma ions.

Due to the higher intensity of the laser pulse, the bubble regime operates with stronger modulations of the electron density and, thus, with higher acceleration gradients. However, when $E \gtrsim E_{l,0}$, the plasma wave becomes highly non-linear (plasma wakefield has no longer a sinusoidal shape) and must be treated nonperturbatively. Examples of the wakefield in the bubble regime in the 2D and 3D geometry can be seen in Figure 1.3 and Figure 1.4, respectively. Although there is no accurate non-linear description of the 3D wakefield, analytical solutions exist in the 1D special case, which can help understand their properties and certain aspects [34], [35]. While the fundamental physics in the 1D case is different, the exact profile of the electric field can also be obtained in the 3D case on the laser axis [36]. The associated electric field is given as $\nabla \mathrm{E} = e\delta n/\varepsilon_0$ or rather as

$$E = \frac{e n_e r_b}{\varepsilon_0}. \tag{1.37}$$

Another key parameter regarding the bubble regime is the radius of the ion bubble r_b. The value of r_b can be estimated by balancing the ponderomotive force

$$F_{\mathrm{pon}} = -\frac{1}{2}m_e c^2 \nabla \frac{a_0^2}{\gamma} = \left| \gamma \approx \sqrt{1 + a_0^2} \approx a_0 \right| \approx \frac{m_e c^2 a_0}{\omega_0}, \tag{1.38}$$

and space charge force of the ionic bubble

$$F_{\mathrm{sc}} = -\frac{e^2 n_e r_b}{\varepsilon_0}, \tag{1.39}$$

which leads to the condition that

$$\frac{m_e c^2 a_0}{\omega_0} - \frac{e^2 n_e r_b}{\varepsilon_0} = 0, \tag{1.40}$$

from which one can obtain

$$r_b \approx \frac{4a_0}{k_p^2 \omega_0}. \tag{1.41}$$

Based on the phenomenological model that has been developed [36], a stable laser propagation in the blowout regime is observed when laser spot size is matched to the bubble, i.e.
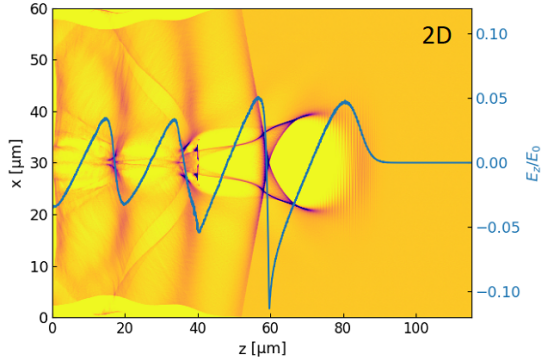
$$k_p \omega_0 \approx 2\sqrt{a_0}. \tag{1.42}$$

Substituting this to (1.41), the radius of the ion bubble can be described as

$$r_b \approx 2\frac{\sqrt{a_0}}{k_p}. \tag{1.43}$$

Moreover, using the equation (1.37) and (1.43), the corresponding field strength can be estimated as

$$E_{\max} = \sqrt{a_0} \frac{m_e c \omega_p}{e}. \tag{1.44}$$

In the 3D nonlinear regime, numerical approach is required, such as commonly used particle simulations [37], [38].

Figure 1.3: Example of the bubble regime in LWFA. Plasma (electron) density profile n_e was obtained from a 2D particle-in-cell simulation using the Smilei code and $a_0 = 4.0$. Normalized wakefield values E_z/E_0 (blue line) are depicted for $x = 30$ μm.
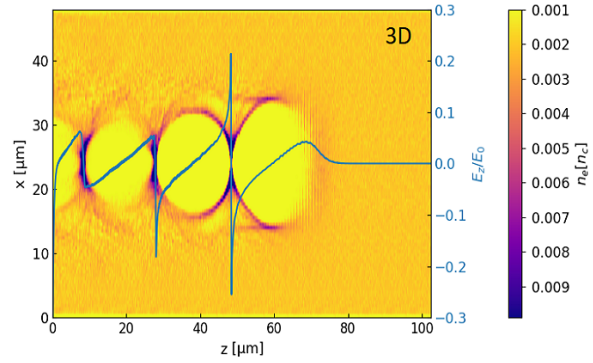
Figure 1.4: Example of the bubble regime in LWFA. Plasma (electron) density profile n_e was obtained from a 3D particle-in-cell simulation using the Smilei code and $a_0 = 4.0$. Normalized wakefield values E_z/E_0 (blue line) are depicted for $x = 24$ μm.

In contrast to the linear regime, the bubble regime of the LWFA provides accelerating and also more significant focusing fields that are transversely uniform. Moreover, these focusing fields can be characterized as linear functions of the radius, pointing to the center of the bubble. Therefore, the electron beam emittance and energy spread growth may be prevented more effectively [26]. Furthermore, the overlap between the focusing and accelerating regions is extended due to the curvature of the wakefield, consequently allowing electrons to be accelerated over a longer distance. In the case of the external injection (described in the next chapter), it is also beneficial for electron trapping [26].

1.11   Limitations of the LWFA on energy gain

1.11.1   Laser diffraction

For any focused Gaussian laser beam in a vacuum, the corresponding spot size evolves as (1.16). Thus, eventually, the diffraction, i.e., spot size expansion, will reduce the laser normalized potential as

$$a \propto \frac{1}{\sqrt{1 + \left(\frac{z}{z_R}\right)^2}}, \tag{1.45}$$

after a certain distance characterized by (1.17). Consequently, reduced effective acceleration length to a few z_R will limit LWFA's attainable energy gain [23].

However, the limitations of diffraction can be reduced, e.g., by optical guiding of the laser beam as a consequence of a lower plasma density on an axis than off the axis [10]. This can be achieved by preformed plasma channels [39], [40] or a adequately strong laser pulse [36]. The latter is particularly referred to as self-guiding [41]. For example, in the 3D bubble regime, the self-guiding conditions can be written as [41]

$$a_0 = \left(\frac{n_c}{n_e}\right)^{\frac{1}{5}}. \tag{1.46}$$

It should be pointed out that in a realistic scenario for high intensities, a relativistic mass increase of plasma electrons has to be taken into account. Moreover, the laser pulse will oscillate in size, while a_0 will change by self-compression and pump depletion [42]. Correspondingly, the plasma frequency becomes radially dependent and can be recast as

$$\omega_p(r) = \sqrt{\frac{n_e(r)e^2}{\gamma(r)\varepsilon_0 m_e}}, \tag{1.47}$$

where relativistic factor is related to the laser strength via $\gamma(r) \simeq \sqrt{1 + a_0^2(r)/2}$.

1.11.2 Electron dephasing

In the laser wakefield acceleration, the phase velocity of the plasma wave v_p, which is approximately equal to the speed of light, coincides with the group velocity of the laser pulse v_g. As a result, electrons trapped in the wakefield can be accelerated to relativistic energies very quickly. Since v_p is usually constant along the acceleration, the electron bunch can eventually overcome the wave phase velocity, and at the end, it can enter the decelerating field of the wakefield and slow down. The maximum achievable energy gain is therefore constrained by this phenomenon. The distance at which electrons can be effectively accelerated is referred to as the dephasing length L_d and can be generally defined as the length at which the electron bunch can travel before it slips by half a period of the wakefield [23]. Depending on the LWFA regime, L_d can be written as

$$\begin{aligned} L_d &\sim \frac{\lambda_p^3}{\lambda_L^2} \qquad \text{for } a_0 \ll 1, \\ L_d &\sim \frac{\lambda_p^3}{\lambda_L^2}a_0 \qquad \text{for } a_0 \gg 1, \end{aligned} \tag{1.48}$$

where λ_L is the laser wavelength.

1.11.3 Laser pump depletion

During the acceleration process, the laser pulse transfers its energy to the wakefield and subsequently to the accelerated bunch. Ultimately, the wakefield amplitude decreases as the laser pulse loses its energy, and the acceleration process can be terminated. The length corresponding to the process in which the laser pulse transfers half of its energy to excite a plasma wakefield is called the depletion length L_{pd} [43].

By analogy with L_d, it can also be written using the ratio of wavelengths and the normalized vector potential of the laser field a_0

$$L_{pd} \sim \frac{\lambda_p^3}{\lambda_L^2} \frac{2}{a_0^2} \qquad \text{for } a_0 \ll 1,$$

$$L_{pd} \sim \frac{\lambda_p^3}{\lambda_L^2} \frac{\sqrt{2}}{\pi} a_0 \qquad \text{for } a_0 \gg 1. \tag{1.49}$$

It is noteworthy that for $a_0 \gg 1$, the pump depletion will generally occur before reaching dephasing (oppositely to the linear regime, considering laser guiding) [23].

Chapter 2

External injection of the electron bunch

2.1 Towards new methods

Since the first proposal of the plasma-based laser-driven acceleration [11], scientists have developed several methods of the electron injection into the laser wakefield. The most straightforward and easiest of them is known as self-injection. It is also the very first method used in experiments and even now for its simplicity. Considering the bubble regime, the principle of the self-injection lies in the fact that during the expulsion of plasma electrons by the ponderomotive force, these electrons stream around the generated bubble, thereby forming a sort of sheath around it. These electrons meet at the back of the bubble, forming a large spatial charge. When the electron density in this region increases beyond a critical value, some electrons are pulled into the bubble in the form of a small bunch. This self-generated and self-injected bunch may then be accelerated in the longitudinal accelerating field, naturally present in the bubble [44]. Several significant discoveries were achieved using this method, such as the acceleration of electron bunch to GeV energies [45]. Moreover, scientists were able to achieve the up-to-date record in accelerating using self-injection. Particularly, they were able to accelerate electron bunch to 8 GeV at a distance of only 20 centimetres [46].

Even though self-injection has proven to be an effective tool for the electron injection in the laser wakefield, overall shot-to-shot instability of the bunches or their insufficient quality limit its use. Broad application of this method is also limited due to its non-linear nature, as even small inhomogeneity in plasma can lead to a premature or delayed injection. This process is also strongly dependent on electron parameters, such as charge, energy, or divergence, which fluctuate, and also on the laser pulse profile. An undesirable characteristic of this method is also the fact that the acceleration process is stopped when the charge of injected electrons becomes larger than the charge from electrons trapped behind the bubble.

In order to achieve better control of the process, scientists have developed several methods that consider different plasma density profiles. Given that a specific plasma density profile can influence the phase velocity of the wakefield, the initiation of the self-injection process can be better controlled. Several experiments considering this relation have been carried out, where decreasing [47] or increasing [48] plasma density, as well as localized plasma density peaks [49], were used. At the same time, it was demonstrated how electron injection can occur by applying an external magnetic field [50].

Throughout the following studies, these methods were supplemented by others, which utilize ionizing and ponderomotive properties of lasers. In some of these methods, the use of an additional laser pulse was suggested. For example, as the driver pulse creates a laser wakefield, this secondary laser pulse can expel plasma electrons into the wakefield by the ponderomotive force. This method is commonly named as the optical injection and can be realized using one laser pulse orthogonally directed to the driver pulse [51] or through the collision of two opposing laser pulses [52].

A method known as the ionization injection, which employs the ionizing properties of the laser pulse, was published at the time when the use of a gas medium with several ionization energies was discussed [51]. As the plasma formed by the laser pulse acts as a background, its electrons from inner shells can be locally ionized at the area of the most intense pulse part and subsequently injected to the bubble. This method has been improved since then and is commonly used in various experiments [53]. The application of the combined methods mentioned above was also studied [54].

Even though these novel methods have helped make important discoveries and elevated plasma acceleration to a higher level, the quality of the accelerating bunch was still noticeably worse compared to that of radio-frequency (RF) accelerators. As a consequence, the objective was to achieve similar or even better results as the Free Electron Laser (FEL) regarding stability and applicability.

2.1.1   Sources of energy spread

For a better understanding of alternative injection methods, it is noteworthy to mention possible sources of energy spread in plasma-based accelerators. The most predominant source is the steep slope of the accelerating fields in the focusing region of the wakefield. Due to the high amplitude and a short period of these fields, this slope arises and causes a longitudinal energy correlation along the bunch. Other less dominant contributions to the total energy spread include the emission of betatron radiation [55], transverse dependence of the beam loading effect in the weakly non-linear and linear regimes [56], and continuous electron trapping in injection schemes [57].

In order to avoid consequences of energy spread, emittance growth, and to compete with FELs, various concepts have been proposed. Concepts that aim to reduce the correlated energy spread take advantage of the beam-induced wakefields [58] or include the use of beam loading, modulated [59] or tailored plasma density profiles [60].

Even though some of these improving concepts have been experimentally studied, the energy spread still remains in the few-percentage range. Thus, the motivation for the improvement of plasma-based accelerators persists.

2.2 The proposal of the external injection

One of the promising alternative methods of the electron injection that can potentially resolve issues with bunch quality is a method known as the external injection. The main principle lies in utilizing a pre-accelerated electron bunch from an external source, such as a conventional RF linear accelerator, and injecting it into an already-created laser wakefield. Since the RF linac provides better control over the accelerating bunch, and its properties can be tailored to a particular plasma acceleration phase, the external injection can deliver better stability over acceleration process.

However, the use of the external injection was doubted at the time of its proposal, as the conditions for its effective use were extremely hard to fulfill. Especially conditions such as size, the momentum of the electron bunch and its synchronization with the wakefield are essential to achieve the successful injection. This method was first experimentally demonstrated in 1993 [61] and subsequently in 1994 [62]. Since then, numerous improvements have been made [63]. Nevertheless, the complete injection of all the electrons into the wakefield was not observed due to the fact that this method is significantly more demanding than all the previously mentioned methods. Considering that the wakefield period is typically only a few tens of femtoseconds short, the size of the electron bunch, together with its synchronization, is required to be below this limit, within a few units of femtoseconds. Such a requirement could not be met from a technical point of view at that time. Nonetheless, several proposals [64], [65], which indicated the possibility of accelerating a short electron bunch with a small energy dispersion originating from a longer external bunch were made. Moreover, these schemes can tolerate larger deviations in synchronization and simultaneously produce electron bunches with a small energy spread [66]. In 2019, almost 100% capture efficiency of the electron bunch was demonstrated [67], and since then, several international projects, such as EuPRAXIA [68], INFN in Italy [69] and others [70], [71], have primarily focused on the external injection method while using RF linac.

In general, there are three techniques to externally inject electron bunches into the wakefield:

- **Behind the wakefield:** In this case, the electron bunch should be delayed by the wavelength of the plasma wakefield [72]. Also, there is an option to inject an electron bunch that is longer than the plasma wavelength. Under these circumstances, the wakefield acts as a bunch slicer since only those parts of the original bunch that are in phase with the plasma wave will be accelerated, while the other parts will be radially dispersed. As a result, a train of short bunches is created and can be accelerated in almost the same phase of the plasma wave. Consequently, they will have approximately the same energy on the exit.

- **In front of the wakefield:** If the electron beam is injected before the laser pulse, the bunch is captured and shortened in the wakefield that has overtaken it together with the pulse [73]. Both methods can produce electron bunches with high energy and small spread compared to the initial pre-accelerated bunch, whose length can be longer than the plasma wavelength.

- **At the angle:** In this case, the electron bunch can be first positioned behind the laser pulse or in front of it before it enters the plasma.

The choice of a specific technique depends on the experimental parameters. Injection in front of the driver pulse generally requires a more powerful laser as well as a relatively short initial external bunch. On the other hand, injection behind the driver pulse requires a less powerful laser, and longer acceleration bunches can be used but their initial energy must be higher. The reason is a lower magnitude of the field, created by the weaker laser pulse, that causes trapping inside the wakefield. For the purposes of this thesis, only the external injection behind the plasma wave will be considered.

2.2.1   Requirements on the electron bunch energy

Assuming a constant plasma density, the total energy gain of plasma acceleration is given as

$$\Delta E = e E_z L_{\text{ac}}, \tag{2.1}$$

where L_{ac} is the acceleration length and E_z is the longitudinal acceleration voltage.

Considering the aspects of dephasing, it is necessary to understand that the external bunch and the wakefield move at different speeds. The velocity of the electron bunch v_e depends on the energy of these electrons and during acceleration approaches the speed of light c. However, the wakefield velocity is constant and is similar to the group velocity of the driver pulse, which can be expressed as

$$v_g = c\sqrt{1 - \frac{\omega_p^2}{\omega_L^2}} < c, \tag{2.2}$$

where ω_L is laser frequency.

To achieve an effective injection of the electron bunch into the wakefield, it is required that the velocities mentioned above are the same at the entrance to the plasma channel [74]. However, during acceleration, the electron bunch velocity increases, approaching c, and thus the condition will be violated, i.e., dephasing will occur. Assuming highly relativistic electrons and $\omega_L/\omega_p \gg 1$, the dephasing length L_d can be approximated as

$$L_d \simeq \frac{\omega_0^2}{\lambda_p \omega_p^2}, \tag{2.3}$$

i.e., the distance by which the electrons are shifted by half a period relative to the wakefield.

Nevertheless, there are several methods, such as the laser optical guiding [75], which reduce dephasing in the plasma channel. These methods are based on the longitudinal modulation of the plasma density, which can increase the acceleration length. It has been also shown that an external bunch with an initial energy of several hundreds of MeV has better control over the space charge force than a less energetic bunch. This force affects the maximum current that can be injected into the wakefield since it is reduced at higher energies.

2.2.2   Requirements on the electron bunch length

One of the main advantages of plasma-based accelerators is the fact that the wakefield acceleration field is located in the plasma. Thus, accelerators of this type can withstand extremely high field gradients. The relation for the cold non-relativistic wave-breaking field provides an estimation of the lower boundary of the field in the plasma wakefield

$$E_0[\mathrm{V/m}] \simeq 96\sqrt{n_p[\mathrm{cm}^{-3}]}. \tag{2.4}$$

In other words, this relation gives an approximate value of the maximum possible wakefield amplitude in the plasma as a function of the plasma density n_p. The wavelength of the wakefield is approximately considered as the plasma wavelength by the relation

$$\lambda_p[\mathrm{\mu m}] \simeq \frac{3.3 \cdot 10^{10}}{\sqrt{n_p[\mathrm{cm}^{-3}]}}. \tag{2.5}$$

If $n_p \approx 10^{16}$ cm^{-3}, then the field gradient can reach $E_0 \approx 9.4$ GV/m. On the other hand, if $n_p \approx 10^{18}$ cm^{-3}, then $E_0 \approx 94$ GV/m. Thus, by increasing the plasma density, the acceleration gradient increases, but the acceleration period shortens. In terms of maintaining an acceptable energy spread of the external bunch and its quality, working with a shorter period of the accelerating field is more challenging. This spread is present because the front and rear of the bunch are subjected to different acceleration fields as a result of slightly different injection phasing. For a fixed field amplitude, the difference in the accelerating field increases with decreasing λ_p. However, such an energy spread can be minimized if the length of the external bunch is much smaller than the period of the accelerating field.

Results of several simulations [76], [77] show that the total energy spread of the electron bunch in the final acceleration stage is proportional to the length of the external bunch during the injection stage. This also implies that the electron bunch size should be smaller than the plasma wavelength. This assumption is also supported by several other concepts [78], [79] focusing on minimalizing the energy spread growth during acceleration. In such a case, an approximately equal acceleration field acts on the external electrons, while transverse forces keep them close to the plasma wakefield axis. As a result, the relative energy spread decreases monotonously during acceleration and can reach a value of around 1% [63].

To obtain a small energy spread, it is also suggested that the initial length of the electron bunch should be much smaller than the dephasing length $L_d \approx \gamma_g^2 \lambda_p$. However, such ultra-short electron bunches require state-of-art accelerators with optimized

compression. Nevertheless, with proper timing, an ultra-short electron bunch of a few femtoseconds can be obtained from a bunch that was several hundreds of femtoseconds at the beginning of the injection. Thereby, these concepts are considered as the most promising.

It may seem that acceleration at low plasma densities would represent a stable solution. On the other hand, the acceleration gradient at such densities is smaller, requiring longer section to obtain the same amount of energy as with higher densities and shorter acceleration sections. The formation of a plasma wave with a large amplitude at low densities also requires a longer laser pulse.

2.2.3   Requirements on the electron bunch charge

When external electrons with a density greater than the density of the surrounding plasma enter the plasma, they start generating their own plasma waves. In a low-density plasma (relative to the electron bunch density), this "additional" wakefield can even be of the same order as the local gradient of the wakefield generated by the driver pulse [70]. This process can be result of the beam loading. Unfortunately, the effect of beam loading can limit the maximum external bunch current that can be accelerated, as well as its resulting quality [36], [80]. To take the advantage of the beam loading effect to minimize the bunch energy spread at the end of the plasma channel, control over the longitudinal beam charge profile is required [81].

In the next sections, two specific phenomena that can generally affect the acceleration of external bunches will be described. Both are related to the region where the vacuum ends, and the plasma begins. The first is ponderomotive scattering, and the second one is vacuum-plasma transition.

2.3   Ponderomotive scattering

Within the theoretical framework, the initial external electron bunch can be approximated as unperturbed. In practice, however, the interaction between the laser pulse and external bunch starts in the vacuum and not in the plasma. Given that the laser pulse travels faster in the vacuum than the electron bunch while taking into account the external injection behind the wakefield, it is necessary for the electron bunch to be localized in front of the laser pulse at a certain distance before entering the plasma (i.e., in a vacuum). Subsequently, the electron bunch will be exposed to a passing pulse at a certain moment in the vacuum. This interaction must be taken into account, since the relativistic ponderomotive force of the laser pulse can disturb the electron trajectories.

The distance from the plasma, when the laser pulse starts to overtake the bunch, is given by

$$L_c = \frac{l}{1 - v_z/c},$$

$$(2.6)$$

where v_z is bunch velocity, l is the distance between the start of the laser pulse and the end of the electron bunch at the entrance to the plasma channel, and c is the speed of light in the vacuum. Since for the relativistic factor of the electron bunch applies

$$\gamma_0^2 = \left(1 - \beta_z^2\right)^{-1} \gg 1, \tag{2.7}$$

where $\beta_z = v_z/c$ is normalized bunch velocity, the equation (2.6) can be recast as

$$L_c \approx 2\gamma_0^2 l. \tag{2.8}$$

For example, if the initial pre-accelerated electron bunch has a kinetic energy of 3 MeV ($\gamma_0 \approx 5.87$) and $l \approx 30$ μm, then $L_c = 2.07$ mm. For comparison, if the Gaussian laser pulse with a waist of $w_0 = 30$ μm and a wavelength $\lambda = 0.8$ μm is assumed. The corresponding Rayleigh length has a value of $z_R = \pi \omega_0^2/\lambda \approx 3.5$ mm. This effectively means that the laser pulse intensity amplitude when the pulse overtakes the electron bunch is almost the same as in its focus. In particular, it has been shown that the ponderomotive force of a relativistically strong pulse $a_0 > 1$ scatters a few-MeV electrons in the direction of the intensity gradient [82]. As a result, the ponderomotive scattering can prevent the injection of the majority of bunch electrons into the wakefield, thus reducing trapping efficiency and worsening the overall quality of the accelerated bunch.

Nevertheless, from equation (2.6), it is evident that as the initial energy of the bunch increases, the laser pulse interacts with the bunch at a relatively greater distance from the focal point. As a result, the effect of ponderomotive scattering can be neglected. Injecting an external bunch into the wakefield at greater distances from the laser pulse can also reduce the ponderomotive scattering since the interaction in the vacuum occurs at a greater distance from the focus, where the effect of the ponderomotive force is smaller. More possible enhancing methods for effective trapping will be discussed later in this chapter.

2.4   The vacuum-plasma transition

As an approximation, it is possible to think of a sharp transition boundary between vacuum and plasma. However, in practice, there is a finite transition region. Within this region (or density ramp), a continuous change in the wavelength or in the density of the plasma is present. As a result, the injected electron beam is affected by the continuously changing plasma wakefield. Consequently, a substantial spread of the external bunch can occur. This phenomenon is significant for high-amplitude wakefields, small initial bunch energies and long transition regions. In this region, especially in the direction of the longitudinal axis, the plasma density n_p increases monotonously. At the same time, the plasma wakefield wavelength gains a spatial dependence while decreasing with the longitudinal direction of the transition region z, since

$$\lambda_p(z) \propto [n_p(z)]^{-1/2}. \tag{2.9}$$

Therefore, at a fixed distance from the laser pulse in the transition region, the plasma wakefield varies as a function of time while the laser pulse travels through

the medium. As a consequence, the injected relativistic electrons in the transition region are affected by the wakefield, which shifts from an accelerating state to a decelerating state and vice versa. Such electrons can therefore be scattered even before they are trapped in the wakefield.

The electrons that are captured are then compressed in both longitudinal and transverse directions. This implies that the plasma wakefield captures external electrons that originate from a relatively long external electron bunch compared to the resulting compressed shape. The length of the trapped bunch l_z is approximately $(\gamma_0/\gamma_g)^2 l_0$, where l_0 is the length of the external bunch before capture and

$$\gamma_g = \left[1 - (v_g/c)^2\right]^{-1/2}, \tag{2.10}$$

is the relativistic factor associated with the laser pulse via the group velocity v_g. With the appropriate choice of the initial electron bunch length, the size of the captured bunch can become smaller than the plasma wavelength λ_p. In particular, if $\gamma_0 \ll \gamma_g \left(\lambda_p/l_0\right)^{1/2}$, then $l_z \ll \lambda_p$.

In order to study the effects of the finite transition from vacuum to plasma on the trapping process of external electrons and their acceleration in detail, several measurements of the longitudinal profile of the electron density were made. In the case of a gas jet with a typical plasma density of $\approx 10^{19}$ cm^{-3}, the size of the transition region was determined to be 200 μm [83] or 400 μm [84]. The results of these measurements, as well as other published studies [85], point to the fact that the effect of the finite vacuum-plasma transition is stronger for smaller initial bunch energies, stronger wakefields, as well as longer transition regions. In such a case, the spread of external electrons occurs, which reduces the overall trapping efficiency. At the same time, the mentioned studies indicate that for laser pulses with a high intensity, there can be a significant decrease in the efficiency of capture even for short transition distances.

2.5   Possible enhancing methods for effective trapping

In order to avoid ponderomotive scattering, Kalmykov et al. [73] proposed the injection at the angle which was previously mentioned. However, in this particular case, the electron bunch is first positioned behind the laser pulse before entering the plasma. Therefore, the bunch still have to propagate through the transition from vacuum to plasma and experience scattering. The following year, Luttikhof et al. [85] proposed an improvement in which the bunch is injected into the wakefield in such a way that it enters the plasma wave from the side. The bunch will start from a zero field and then interact with the wakefield of constant wavelength but increasing in strength, where the plasma density is already at its maximum value. Thus, the electron bunch will not experience any interaction with the wakefield in the transition region.

Other results from 2007 [86] show the following. If the electron beam is injected into the plasma at larger distances from the laser pulse, then the effect of ponderomotive scattering is small, and at the same time, the trapping efficiency is greater due to changes in the structure of the wakefield. However, the energy spread is considerably greater than at smaller distances. This is also related to the size of the electron bunch in the longitudinal direction, which increases the overall distance l. At the same time, the energy gain is typically in the order of several hundred MeV [87].

In an attempt to increase the trapping efficiency while keeping the energy spread as small as possible, it is possible to use a laser pulse with a spot size much larger than the size of the injected bunch. As a result, the injected electrons will be located near the axis of the laser pulse, where the transverse component of the ponderomotive force is small. Thus, the effect of the ponderomotive scattering will also be small. Nevertheless, this method requires a very intense (petawatt level) laser pulse. Nowadays, however, with the development of high-power lasers, it is already possible to generate electron bunches that meet this requirement. Even their length can be smaller than the plasma wavelength, thus contributing to a smaller energy spread. At the same time, it reduces the strict requirements for the distance between the electron bunch and the laser pulse before entering the plasma. Moreover, it is possible to consider a wider range of the energies of the initial bunch without significant effects of ponderomotive scattering.

Another possible way to increase the trapping efficiency is to increase the charge of the external bunch. However, the results show [86] that at higher initial charge values, the "resulting" transverse size of the electron bunch is also larger. This is caused by the increasingly dominant effect of the Coulomb repulsion, especially at lower initial energies of the electron bunch, leading to a worse trapping efficiency and greater energy spread.

It is evident that the effective wakefield acceleration is directly related to the injection energy, the amplitude of the laser pulse as well as the wakefield, and to the parameters of the accelerated bunch, while all these quantities are interconnected. There are a few other methods that can provide better and more consistent results. In the following subsections, two of them will be described.

2.5.1   Beam matching

Matching of electron beams into the focusing fields of plasma wakefield is essential for conserving their emittance and overall quality. These effects are generally caused by a non-zero bunch length or a non-zero energy spread. It has been observed that rapid increase in energy spread can occur during acceleration [5], [88] as well as after it, during bunch transport [3], [89]. Results of several studies show that beam matching reduces emittance growth from finite energy spread [88] and mitigates energy loss and correlated growth of energy spread due to the emission of synchrotron radiation [90].

In order to understand the origin of the emittance increase and the fundamental bunch dynamics behind it, one can consider a simplified beam envelope equation with a uniform focusing field with gradient K and no acceleration [3]. Particularly,

$$\sigma_x'' + \left(k_\beta^2 - \frac{1}{\beta^2}\right)\sigma_x = 0, \qquad k_\beta = \sqrt{\frac{e\gamma}{mc^2 K}}, \qquad \beta = \frac{\sigma_x^2 \gamma}{\epsilon_n}, \qquad (2.11)$$

where σ_x is the transverse bunch size, k_β is the betatron wavenumber, β is the beta function of the beam, γ is its relativistic factor, and ε_n is the normalized emittance. The beta function is a measure for the bunch size and for the betatron length, γ is a measure for the spread in the particle slopes. Considering transverse particle position x and slope of a particle trajectory $x' = \mathrm{d}x/\mathrm{d}z = p_x/p_z$, then alpha function

$$\alpha = -\frac{\langle xx'\rangle}{\varepsilon_n}, \qquad (2.12)$$

can represent the correlation between x and x' e.g., at beam waist $\alpha = 0$. The general solution of equation (2.11) expresses the beam envelope's oscillating nature when the beam's elliptic shape rotates in the phase space. In other words, while the electron bunch is being accelerated, the individual particles perform transverse betatron oscillations with a frequency of

$$\omega_\beta^2 = \frac{K^2 \omega_p^2}{\gamma_{\mathrm{L}}}\sin(k_p\xi), \qquad (2.13)$$

where γ_{L} is the Lorentz factor, and $\xi = z - v_g t$ is the comoving variable. Given that the betatron frequency is ξ-dependent and the electron bunch may have an energy chirp, the individual longitudinal slices of a finite length bunch will oscillate at different frequencies, leading to a ξ-dependence of the betatron oscillation phase. Subsequently, this leads to complete decoherence during the acceleration process. This effect is illustrated in Figure 2.1, where the phase-space ellipses of longitudinal bunch slices are shown for different z positions.
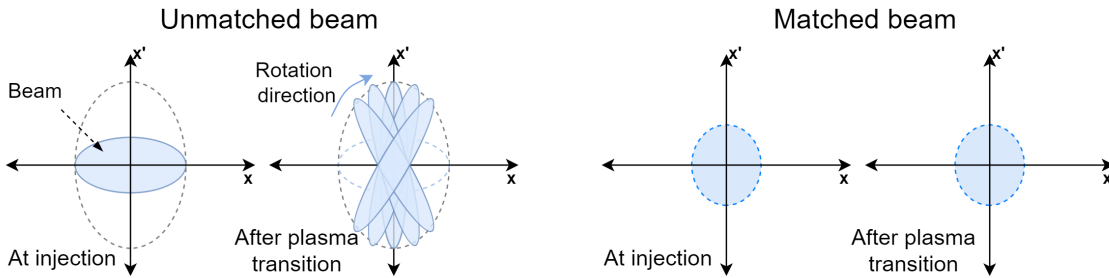
Figure 2.1: Difference between an unmatched (left) and matched (right) externally injected beam with a large correlated energy spread during phase-space evolution inside a plasma stage. Effects of energy gain are neglected.

Nevertheless, the relation (2.11) implies that the oscillations of the bunch envelope can be suppressed if $\beta = k_\beta^{-1}$, which for constant K suggests that $\alpha = -\beta'/2 = 0$. In such a case, the beam is considered to be matched to the focusing fields in the plasma. This implies that the increase in emittance is thus effectively suppressed. This also applies to a situation where the energy spread is substantial.

Further study shows [5] that even adiabatic changes to K and γ will not disturb the matching conditions and thus not lead to emittance growth. The transverse normalized emittance, which is a figure of merit for the beam quality, is defined as

$$\varepsilon_x = \frac{1}{m_e c}\sqrt{\langle x^2 \rangle \langle p_x^2 \rangle - \langle x p_x \rangle^2}, \qquad (2.14)$$

where $\langle \rangle$ represents an ensemble average over the bunch distribution, x is the transverse position, and p_x is the transverse momentum.

In the case of the unmatched or mismatched beam, slice ellipses in the phase space develop a tilt with respect to each other, increasing the projected area [91]. Consequently, the projected emittance increases. Emittance growth due to the beam's elliptic shape rotation in the phase space is theoretically reversible [92]. However, recovering the emittance by further rotation in a subsequent plasma stage is not realizable by any combination of beam optics.

Several methods have been proposed to effectively reduce bunch divergence and thereby suppress the increase in emittance. One of the possibilities is to place the focusing element as close as possible to the plasma exit. It can be realized with plasma lenses that take advantage of the driver laser pulse used for acceleration [93] or that are driven by a discharge [94]. As a result, the emittance growth in both planes can be effectively reduced. Another method that proved to be effective in reducing bunch divergence includes appropriately tailored plasma-to-vacuum transitions so that the focusing fields affecting electron bunch will gradually decrease [95], [96].

2.5.2 Tailored plasma density profiles

As indicated above, demanding conditions are put on the beta function during injection due to the strong focusing fields. For instance, if the initial bunch energy is ~ 100 MeV and plasma density is $n_e = 10^{17} \mathrm{cm}^{-3}$, then is required that $\beta \simeq 0.3$. Such sub-mm values of the beta function are very difficult to achieve with conventional methods and normal focusing elements used in linacs [71]. For this reason, beam matching is particularly important in the case of external injection. This can be achieved by properly tailored density transition. Density ramps at the beginning of the acceleration as well as down-ramps at the exit are able to meet the conditions for the correct beam matching even for a larger beta function, which will gradually decrease with increasing focusing fields.

On the other hand, a general cause of the large energy spread is the short wakefield wavelength (~ 10 μm) and high amplitude (~ 10 GV/m) of the accelerating field in the plasma. The combination of these two factors leads to a longitudinal energy correlation, i.e., energy chirp in the direction of the accelerated bunch. Therefore, an adiabatic reduction of the focusing forces at the plasma-vacuum transition is thus desired. It has been demonstrated [97] that the linear energy chirp can be compensated if the acceleration length is tuned closely to the dephasing length.

Such an adjustment can be achieved by changing the plasma density [98]. However, it should be noted that this will also affect laser propagation, plasma wake formation, and the electron injection.

In recent theoretical work, different methods of longitudinal plasma density tailoring and their influence on the electron bunch properties were discussed [99]. These techniques were then applied in experiments. Based on the results, it was suggested to use a transition to higher plasma density to increase the acceleration of the rear part of the bunch. At the same time, the front is less accelerated and later decelerated. Consequently, the electron bunch will rotate in the $(z; p_z)$ phase space. Since the bunch energy is predominantly given by the longitudinal momentum p_z, this reduces the energy chirp as well as the energy spread [100]. Further studies based on simulations support the conclusion that the energy spread reduction observed in the experiment is due to a significant decrease in the energy chirp [60].

A different study [96] discussing the relevancy between the external injection and properly tailored plasma density ramps, including staged accelerator schemes, indicates that for larger initial electron bunch energies as well as larger energy spread, the plasma ramp is required to be longer. This is in order to maintain adiabaticity at higher energies and also to maximize the beta function, as mentioned above. Moreover, such modification minimizes divergence in the drift before the plasma section, thus preventing chromatic emittance growth. It is noteworthy that this study also suggests shorter plasma entrance ramps than the exit down-ramps. This is because the injected electron energy is longitudinally much smaller before acceleration. And eventually, the ramp profile should follow the design of the down-ramp.

Another study [95] focused on the evolution of both β and α functions between two plasma stages that require exact beam as well as adiabatic matching. Results show that perfect matching can be obtained even for short longitudinally tailored plasma sections (nonadiabatic profiles). Consequently, the theoretical formalism applies for short or long sections where the adiabatic approximation is reasonable.

Chapter 3

Particle-In-Cell simulations of laser wakefield acceleration

3.1 General history and purpose

Generally, complete analytical solutions for most complex physical problems are sometimes impossible to obtain. For this reason, using numerical analysis in solving complex equations with the help of powerful computers is today's standard in every branch of physics, as well as in plasma physics. Additionally, these simulations represent a convenient way to test both theories and large construction experimental projects before they are realized.

Simulations of laser-plasma interaction together with the particle-in-cell (PIC) method were developed simultaneously with the concept of plasma-based laser-driven acceleration. The numerical methods for laser-plasma physics were developed already at the end of the 1950s. One of the first scientists who noticed the potential of computer simulations in this field was J. Dawson. In order to calculate the trajectories of the charged particles for electrostatic problems in 1D, he developed the concept of the "charge-sheet," a substance for real particles that normally interact with one another via Coulomb forces [101]. However, in the following years, scientists realized that Dawson's concept required a significant amount of computing power. As a result, a computational grid and the concept of particles interacting with this grid rather than one another were proposed [102]. This approach was employed in place of electromagnetic fields, the Maxwell equations, and the Coulomb equation.

Later in the 1970s, the theory of numerical plasma modelling was developed based on finite-size particles and the grid that these particles interact with. A few years later, K. Birdsall and B. Langdon co-wrote "Plasma Physics via Computer Simulation", a book that summarized all the advancements made up to that point in the area and established the PIC method in plasma simulations [103].

During the last two decades, laser-wakefield accelerators have substantially evolved to the extent of producing quasi-monoenergetic electron beams with the energy at a GeV level [45]. With technological progress and an increase in computing power, this progress was also made possible thanks to particle-in-cell simulations and their ability to reproduce or predict the properties of the captured charged particles in the plasma wakefield, such as their total charge, emittance, mean energy, and energy spread. Moreover, upgraded algorithms for better and faster performance made improving their accuracy and implementing features such as collisions through Monte-Carlo method possible [104].

3.2   Basic principle of PIC

There are various approaches to model plasma, and it might depend on a number of different parameters [105]. Despite today's powerful computing capabilities, it is not possible to effectively simulate a plasma system that would typically contain $\sim 10^{20}$ electrons and ions. Fortunately, in the field of plasma physics, the main subject of investigation is usually not the interaction between particles but rather the collective effects of plasma. Therefore, multiple real particles can be represented as a computational particle with a finite size. This alternative was proposed as soon as plasma simulations were considered. With this substitution, it is possible to filter out the effect of the shorter-range force, thereby allowing the use of a much smaller number of particles with results corresponding to observable macroscopic plasma phenomena [106]. Computational particles are more often referred to as either macro-, pseudo-, or quasi-particles.

In the case of the particle-in-cell method, it is considered that charged macro-particles do not interact directly with each other but with the computational mesh. The magnetic and electric fields are calculated at the points of this mesh, and then an electromagnetic force is applied to each particle depending on their individual positions. The computational mesh in most PIC codes is Euler orthogonal and is typically referred to as a grid [102]. As aforementioned, plasma usually contains a lot of particles; thus, a statistical approach can be applied. This approach is typically referred to as kinetic theory in which the distribution function $f(\mathbf{x}, \mathbf{p}, t)$ is introduced. Since the grid contains a finite number of macro-particles, this function is discrete. Including complete information about the state of the system, $f(\mathbf{x}, \mathbf{p}, t)$ also describes its evolution in time through 7 unbounded degrees of freedom. Generally, three spatial, three for velocity and one temporal are included. Therefore, the particle-in-cell method principally combines the kinetic and electromagnetic theory of the plasma.

It is noteworthy that particular techniques are more preferred based on the different spatial and temporal scales. For example, at the smallest scales, e.g., in femtosecond scales, one can use the particle-in-cell method, while at large scales, the magnetohydronamics (MHD) approach can be applied, where plasma is treated as a fluid [107]. At intermediate scales, the hybrid methods are often used to explore slower phenomena and accelerate the evolution of the system by making specific assumptions [108].

3.2.1 Kinetic theory

The kinetic description of the collisionless plasma is based on the solution of the hyperbolic partial differential equation known as the Vlasov equation, which describes the time evolution of the distribution function $f(\mathbf{x}, \mathbf{p}, t)$ [7]. It can be defined as

$$\left(\frac{\partial}{\partial t} + \frac{\mathbf{p}}{m_s \gamma} \cdot \nabla + \mathbf{F}_L \cdot \nabla_{\mathrm{p}} \right) f(\mathbf{x}, \mathbf{p}, t) = 0, \tag{3.1}$$

where

$$\mathbf{F}_L = q_s \left(\mathbf{E} + \mathbf{v} \times \mathbf{B} \right), \tag{3.2}$$

is the Lorentz force acting on charged particles inside collective electric $\mathbf{E}(t, \mathbf{x})$ and magnetic $\mathbf{B}(t, \mathbf{x})$ fields. $\mathbf{x}$ and $\mathbf{p}$ denote the position and momentum of a phase-space element, respectively. Relativistic Lorentz factor γ and particle velocity $\mathbf{v}$ have the following form

$$\gamma = \sqrt{1 + \left(\frac{\mathbf{p}}{m_s c} \right)^2} \quad \text{and} \quad \mathbf{v} = \frac{\mathbf{p}}{m_s \gamma}, \tag{3.3}$$

and index s represents given species consisting of particles with charge q_s and mass m_s.

3.2.2 Electromagnetic theory

Since in the particle-in-cell method, the plasma is treated as a statistical sample of charged particles, the dynamic evolution of the system can be described with the use of Maxwell's equations:

$$\nabla \cdot \mathbf{B} = 0, \tag{3.4}$$

$$\nabla \cdot \mathbf{E} = \frac{\rho}{\varepsilon_0}, \tag{3.5}$$

$$\nabla \times \mathbf{B} = \mu_0 \left(\mathbf{J} + \varepsilon_0 \frac{\partial \mathbf{E}}{\partial t} \right), \tag{3.6}$$

$$\nabla \times \mathbf{E} = -\frac{\partial \mathbf{B}}{\partial t}, \tag{3.7}$$

where ε_0 is the vacuum permittivity, μ_0 is the vacuum permeability. Charge density ρ and current density $\mathbf{J}$ can be derived from the particle distribution function

$$\rho(\mathbf{x}, t) = \sum_s^{N_s} q_s \int \mathrm{d}^3 \mathrm{p} f_s(\mathbf{x}, \mathbf{p}, t), \tag{3.8}$$

$$\mathbf{J}(\mathbf{x}, t) = \sum_s^{N_s} q_s \int \mathrm{d}^3 \mathrm{p} \mathbf{v} f_s(\mathbf{x}, \mathbf{p}, t), \tag{3.9}$$

where N_s is total number of macro-particles.

3.2.3   PIC algorithm

As indicated above, each macro-particle represents a particular amount of real physical particles. Therefore, the PIC method requires a weighting scheme to build the charge and current densities on the grid and to project forces found on the grid back to the particles. The main computational cycle of the PIC method, as depicted in Figure 3.1, consists of four fundamental steps. Namely, the weighting of particle quantities to the grid, solving the field equations on the grid, projecting forces back to the particles, and advancing particle trajectories [109].
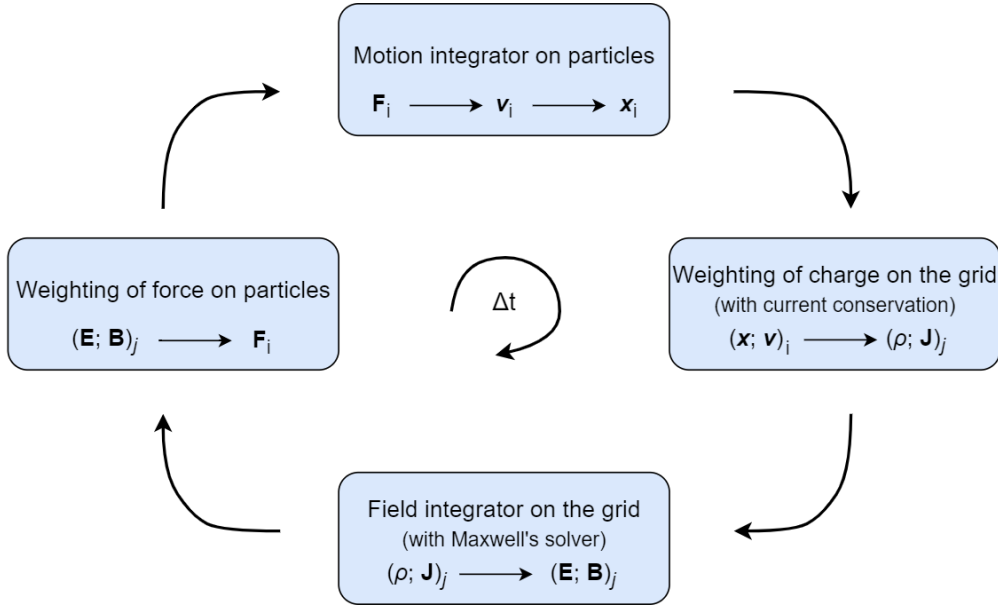
Figure 3.1: Computing algorithm for particle-in-cell method. Indices i and j represent i-th and j-th point of the grid.

The charge of macro-particles is essentially the charge that has been smoothed over the grid cell since they are weighted to the grid points. By using shape-functions $S(x_j - R_g)$, where x_j is the position of j-th particle and R_g is the position of the grid point defined by the weighting method, the macro-particles can therefore overlap with one another.

Shape functions of macro-particles, particularly the spatial shape function and the velocity shape function, have a finite size and, therefore, can be described mathematically. In the case of the velocity shape function, the choice is almost always the Dirac's delta function [110]. Such an option also applies to spatial shape function. Nevertheless, modern PIC codes such as Smilei prefer b-spline functions; see Figure 3.2 [7].
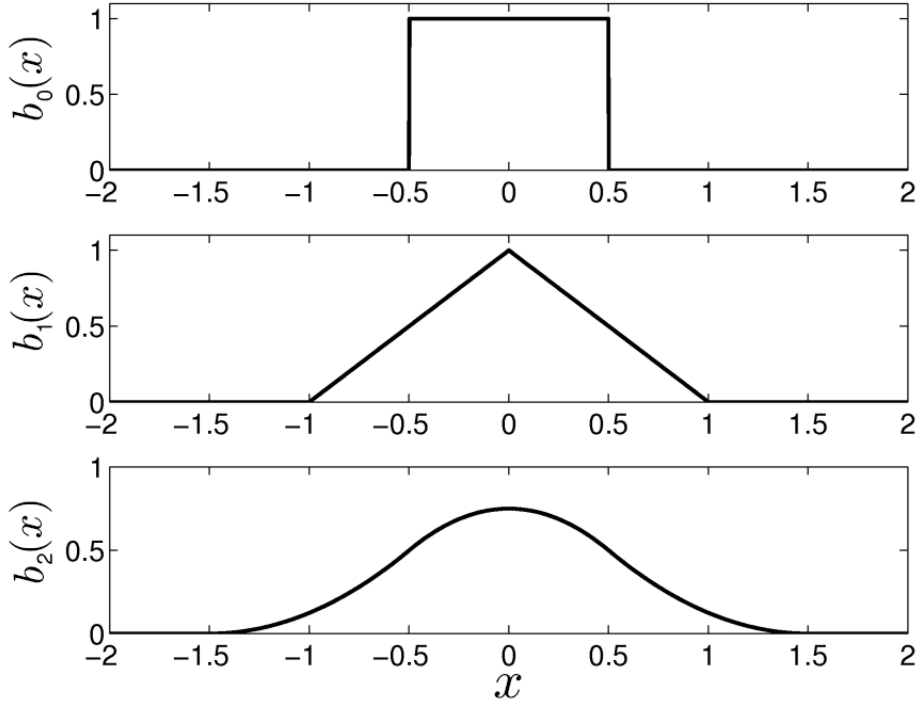
Figure 3.2: B-spline functions of the first three orders.

The standard option of the Smilei code is linear weighting using $b_1(x)$ as a spatial shape function. The corresponding b-spline function has a triangular shape and is defined as

$$b_1(x) = \begin{cases} 1 - \frac{|x|}{\Delta x} & \text{if } |x| \leq \Delta x \\ 0 & \text{otherwise.} \end{cases} \tag{3.10}$$

However, Smilei also allows changing the interpolation order, i.e., the b-spline function through a python script [7].

3.2.4 Field solvers

Generally, the choice of a particular field solver depends on the boundary conditions of the simulation box. The very first PIC codes developed in the 1960s [106] used Fast Fourier Transform (FFT) to solve field equations [103]. However, these are global methods since information about fields from all over the simulation box is required, as well as data interchange between different domains. As a result, global methods often struggle with inefficient parallelization.

Nowadays, field equations are usually solved by Finite-Difference Time-Domain (FDTD) method, where the field equations are discretized on a spatial so-called Yee grid [111]. Due to data path minimization requirements, local techniques can be implemented. In order to achieve the second order accuracy in current density calculations, Yee proposed to distribute field components in space with a distance between them representing half of a grid cell. Furthermore, computing is distributed partly in the middle of cells and partly on the edges.

Massive parallel PIC codes can alternatively use the density decomposition technique [112]. A significant advantage of the density decomposition is the implementation of the continuity equation for calculating the current onto the grid. As a result, the divergence equations (3.4), (3.5) can be used only as initial conditions in the beginning and then skipped. Therefore, the preliminary updating of fields is greatly simplified.

3.3 Numerical instabilities of PIC simulations

PIC simulations are subject to various numerical instabilities, which can introduce artificial bias and consequently alter their results. In this section, the basic principles of the two most common numerical instabilities in PIC simulation will be described. Particularly, numerical heating and numerical Cherenkov instability.

3.3.1 Numerical heating

The effect of numerical heating is a well-known complication of standard PIC codes. There are two distinct sources of numerical heating. The first comes from the application of macro-particles. Particularly, each cell generally contains a small number of macro-particles. However, the movement of even one macro-particle between cells can result in substantial fluctuation within the electric fields. This can lead to the artificial production of electromagnetic radiation that stochastically heats the neighbouring plasma particles [113].

The second source of numerical heating originates from the use of the grid, especially from the effects of the aliasing of plasma waves [103]. If it's unable to represent waves of higher frequencies on a discrete grid, they are merged with the waves of lower frequencies, which leads to grid aliasing. In practice, if the condition

$$\Delta x \leq \pi \lambda_{\mathrm{D}}, \tag{3.11}$$

is not satisfied, where Δx is spatial step, modes that are not affected by Landau damping are aliased with modes that so. Given that the energy of plasma wave loses is not the same as the energy which macro-particles receive, this consequently leads to numerical heating [103]. On the other hand, if condition (3.11) is not satisfied, non-physical numerical heating will grow exponentially until the effective Debye length becomes comparable with the grid size. Subsequently, the exponential growth transitions to more tolerable linear heating.

The electrostatic part of the code is generally considered as most prone to cause numerical heating, considering the fact that electrostatic plasma waves are responsible for the Debye shielding (i.e., a possible source of the inconsistent interpolation of the fields defined on the grid to the particle position).

In order to increase the Debye length and resolve the problem with grid spacing, thus overcoming numerical heating, a warm plasma model can be applied [114]. Moreover, it has been shown that higher order shape functions [115] and current smoothing [116] can substantially reduce the effect of grid aliasing.

3.3.2 Numerical Cherenkov instability

A recent study conducted in 2013 [117] pointed out that while PIC simulations of LWFA are able to reliably predict very low emittances of electron bunches with small charge ($\sim$ 1 pC) [5], [118], they tend to overestimate transverse emittance to a great extent in the case of a bunch with a charge of tens of picocoulombs or more. It is known that numerical heating can cause similar growth. However, in this study, it was demonstrated that the dominating effect causing the emittance growth of bunches with larger charges is numerical Cherenkov radiation.

The effect of numerical Cherenkov radiation (or instability) was first described in 1974 by B. Godfrey [119] as a result of the FDTD Yee scheme with the combination of its feature that the numerical velocity of electromagnetic waves in a vacuum is lower than the speed of light. Because of this, macro-particles can travel faster than these waves and thus can emit artificial Cherenkov radiation with a high frequency (similar to the real case, hence the name).

One of the most straightforward techniques to mitigate numerical Cherenkov instability is to choose extremely small grid cell sizes [119]. Nevertheless, as indicated above, this approach can adversely affect the growth of numerical heating. Other methods include low-pass filters [120], [121] or modified computational scheme [122], [123]. It has been also suggested to moderately increase the speed of light in Maxwell's equations [124]. None of these approaches, however, is particularly well adapted to the characteristic of the laser wakefield acceleration in the laboratory frame. For example, regarding low-pass filters, the physics at lower frequencies are unavoidably impacted by any filtering procedure in real space (as opposed to Fourier space) that significantly reduces high-frequency radiation. However, this is in direct conflict with lasers used in laser wakefield acceleration, which generally have a high frequency, making it impossible to filter Cherenkov radiation. As a solution, a study mentioned at the beginning of this subsection proposed a new computational scheme of a higher order than Yee [117]. The method is also known as the Lehe scheme. It was already implemented in the Smilei, and it results in an efficient suppression of Cherenkov radiation and a noticeable reduction of emittance growth.

3.4 Grid computing

A distributed architecture with numerous computers linked by networks and working together to complete a single task is referred to as a "grid". The term grid computing became relevant when I. Foster and C. Kesselman published their seminal work [125] in 1999. Particle-in-cell simulations are significantly computationally demanding and

almost impossible for a single machine to handle. However, with the help of several machines on a network cooperating under a standard protocol, working as a single virtual supercomputer, this complex task can be executed in a relatively short period of time.

Every computer connected to the grid network runs specialized software to make grid computing work. All of the grid's tasks are coordinated and managed by this software. In principle, it divides the primary task into smaller tasks and assigns a smaller job to each computer. Furthermore, computers can communicate and exchange data on the part of the subtasks being completed in parallel. As a result, the computers can combine their efforts and provide a combined output for the given primary task. After the subtasks are finished, the results from every machine are combined in order to complete the primary task.

A typical grid computing network contains of three machine types:

- **Control node/server:** Also known as the scheduling system or Batch Jobs System (PBS). Its purpose is to administer the entire network and keep a track of the grid's resources, such as memory usage, CPU time or disc space. If there are not enough resources, the scheduling system will keep the computational jobs waiting in queues and will gradually release them to run.

- **Provider/grid node:** Also known as a computational node. It represents a computer that contributes its resources to the resource network, i.e., does the computation itself. The network can consist of many grid nodes.

- **User:** It refers to the computer that utilizes the resources on the network to complete the task. It prepares and submits jobs on so-called frontends, which are, in principle, machines reserved for the user activity.

The advantage of the Smilei PIC code, regarding grid computing, is that it uses OpenMP [126] and MPI [127] for parallelization. Thus, the computations are effectively speeded up. Furthermore, Smilei uses dynamic load balancing, which significantly improves performance. This approach periodically exchanges the segments of the simulation box between MPI processes. As a result, each MPI process owns a fair amount of the simulation load. Smilei computational performance has been recently enhanced with vectorized operations, particularly the projection of currents and the interpolation of fields [7].

One of the largest providers of grid computing in the Czech Republic is a virtual organization called MetaCentrum. Its primary purpose is managing distributed computing infrastructure consisting of computing and storage resources owned by CESNET and co-operative academic centres within the Czech Republic. Grid graphics of MetaCentrum CESNET can be seen in Figure 3.3.
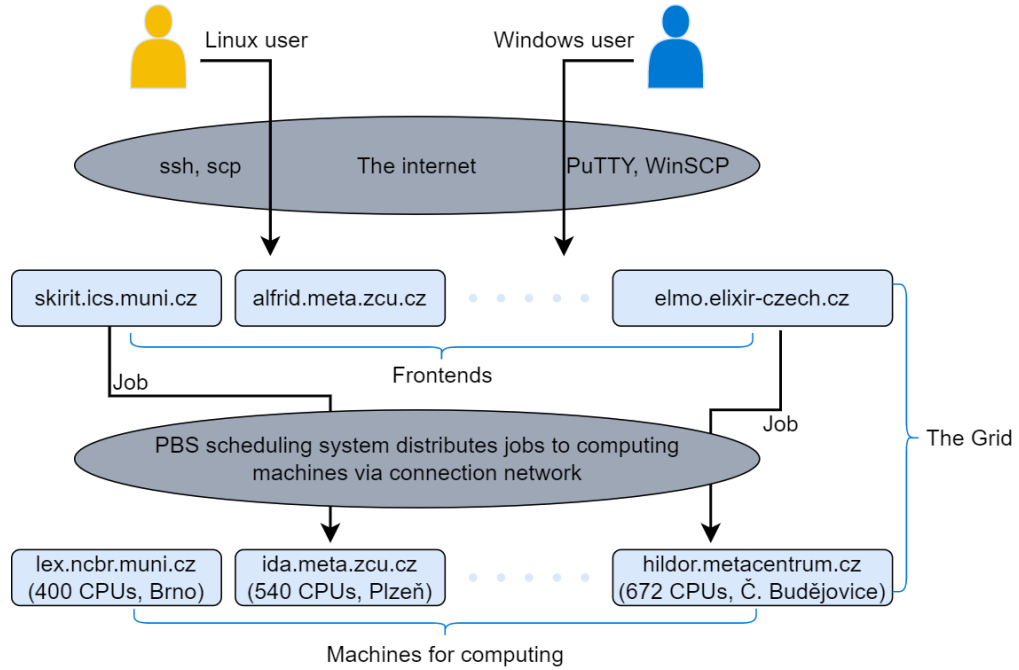
Figure 3.3: Grid graphics of MetaCentrum CESNET.

CESNET is an association of universities of the Czech Republic and the Czech Academy of Sciences. It operates and develops the national e-infrastructure for science, research, and education, which encompasses a computer network, computational grids, data storage and a collaborative environment.

All 2D simulations carried out in this work were accomplished using computing infrastructure operated by MetaCentrum. Nevertheless, based on performed test runs, a typical 3D simulation of LWFA with external injection is significantly more computationally demanding. For instance, such a simulation with the LWFA duration of only ~ 0.5 ps requires ~ 9900 core hours. However, in order to fully capture the electron beam evolution after the plasma entrance, each of these simulations should correspond to at least 3 ps of beam acceleration; thus, each requires ~ 60000 core hours. Therefore, the use of 1 080 000 CPU core hours in the frame of the project was expected. These requirements are too demanding to fulfil within the MetaCetrum infrastructure. Due to this, all 3D simulations in this work were executed via IT4Innovations National Supercomputing Center [128] at the Technical University of Ostrava. IT4Innovations operates the most powerful supercomputing systems in the Czech Republic and is made available to Czech and foreign research teams from academia and industry. Together with the CESNET and CERIT-SC institutions, IT4Innovations constitutes e-INFRA CZ.

Chapter 4

Simulation results: External injection and the effect of different plasma density profiles

4.1   Simulation setup

In order to understand the possible effects of different plasma density profiles used in combination with the external injection, 2D and 3D particle-in-cell simulations using the Smilei code [7] were performed. The simulation setup is shown in Figure 4.1. An external electron bunch trailing behind a laser pulse was directed into the plasma with a density ramp at the plasma front followed by uniform electron density $n_e = 3.5 \cdot 10^{18}$ cm^{-3}. The spatial and temporal envelope of the driver pulse as well as the electron beam were chosen to have Gaussian profiles. The duration and transverse size of the electron bunch in Table 4.1 correspond to the standard deviation of the normal distribution. The bunch is monoenergetic. The group velocity of the driver pulse was $\sim 0.99899c$, and the velocity of the simulation window v_w was adjusted accordingly (see Table 4.1). Two specific plasma density profiles were used, namely: linear and convex parabolic. For each profile, 8 different ramp lengths L_r were used 25 μm, 50 μm, 75 μm, 100 μm, 200 μm, 300 μm, 400 μm, 500 μm, and 700 μm. The total number of particles in the electron bunch in 2D and 3D simulations was 50 000 and 5 000 (approximately 10 and 7 particles per cell), respectively. The rest of the most important simulation parameters is shown in Table 4.1.
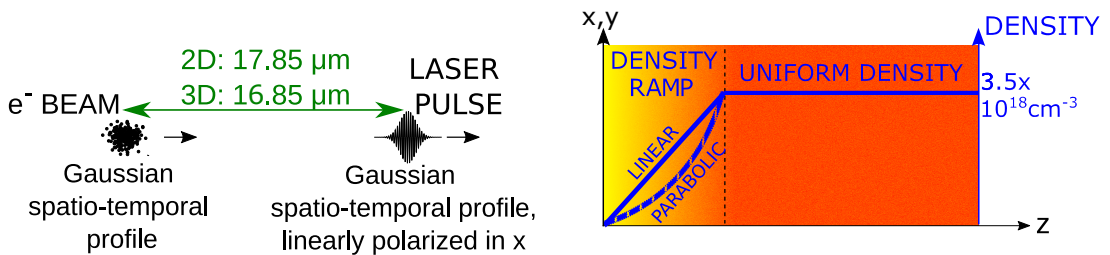
Figure 4.1: Schematic representation of the initial phase of the simulations with the linear (blue solid line) and parabolic (blue dashed line) plasma density ramp.

Laser pulse	
Wavelength λ_L	800 nm
Duration (FWHM)	30 fs
Waist	9 μm
Normalized field a_0	4.0
Focal area position z_0	0 μm
Electron bunch	
Duration σ_z	1.0 fs
Transverse size $\sigma_{x,y}$	0.6 μm
Energy	100 MeV
Relative energy spread $\Delta E/E_{mean}$	1.0 %
Charge	5.0 pC
Transverse emittance $\varepsilon_{x,y}$	0.1 mm·mrad
Simulation parameters	
Time T_{sim}	3.0 ps
Longitudinal window size	115.2 μm (2D), 102.4 μm (3D)
Transverse window size	60.0 μm (2D), 48.0 μm (3D)
Window velocity v_w	0.99899c
Plasma particles per cell	4 (2D), 2 (3D)
Critical density n_c	$1.7 \cdot 10^{21}$ cm^{-3}

**Table 4.1:** Initial parameters used in both 2D and 3D simulations.

One of the useful features of the Smilei code is the ability to track electron bunch particles separately. Diagnostics of generated fields and injected electrons was evaluated every 0.03 ps. In order to save computational time, a moving window was used. $\xi = z - v_w t$ is a coordinate moving with the simulation window.

As shown in Figure 4.1, in the 2D simulations, the distance between the pulse and electron bunch is $s_{2D} = 17.85$ μm, which corresponds to the plasma wavelength λ_p. This value was computed using equation (1.27) in subsection 1.8 together with equation (2.2) in subsubsection 2.2.1. However, due to different and more precise focusation of the driver pulse in 3D simulations [129], the distance has to be set to $s_{3D} \sim 16.85$ μm. Such an adjustment was concluded based on previous test simulations that were performed. Otherwise, the electron bunch would escape from the bubble. One of the explanations for the different distances between the laser pulse and the electron beam is the shape of the bubble itself. Figures 1.3 and Figure 1.4 show that a bubble in 2D geometry has an elliptical shape, or rather an elongated shape in the longitudinal direction. On the other hand, a bubble created in 3D simulation has an almost spherical shape since the equations for the wakefield themselves are different [130]. This means the length range for effective injection inside the bubble is different for 2D and 3D geometry.

4.2   Results of 2D simulations

As mentioned above, due to differences between 2D and 3D simulations, which also result in different wakefield amplitudes [130], 2D simulations were performed only to make initial assumptions as they are much less computationally demanding.

In order to investigate the effects of different profiles and lengths of the plasma ramp, data about the mean energy E_{mean}, energy spread ΔE (computed as weighted standard deviation), relative energy spread $\Delta E/E_{mean}$, and transverse emittance ε_x that were influenced by the uniform plasma density were primarily studied. These properties were therefore firstly examined until the end of each ramp. As Figure 4.2 shows, for an electron bunch travelling in a 700 μm long density ramp, there are eight measurements at each position that correspond to the ends of the remaining shorter ramps. At the same time, for a bunch travelling in a 25 μm long density ramp, the measurement was made only at $z \sim 25$ μm, because beyond that, the bunch is already in a uniform density.
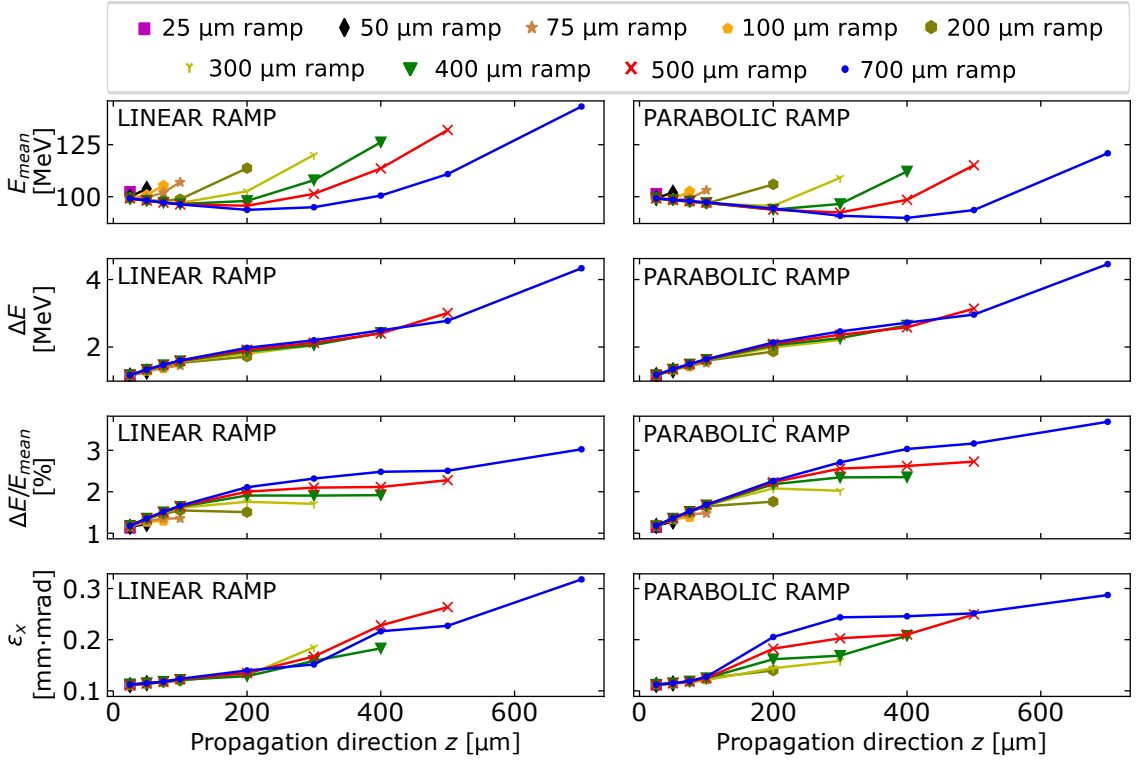
Figure 4.2: Evolution of the electron bunch energy E_{mean}, energy spread ΔE, relative energy spread $\Delta E/E_{mean}$, and transverse emittance ε_x for different ramp types is shown until each of the ramps respectively ends.

Based on Figure 4.2, the first conclusions can be made. It can be assumed that the examined properties of the electron bunch do not significantly depend on the length and profile of the ramps during the first 100 μm of the propagation. A closer observation of this area was made (see Figure 4.3), supporting this assumption, although $\Delta E/E_{mean}$ is arguably lower in some cases for linear and parabolic profiles of specific shorter lengths (50, 75, and 100 μm) from $z \sim 50$ μm to 100 μm, compared to the longer ramps.
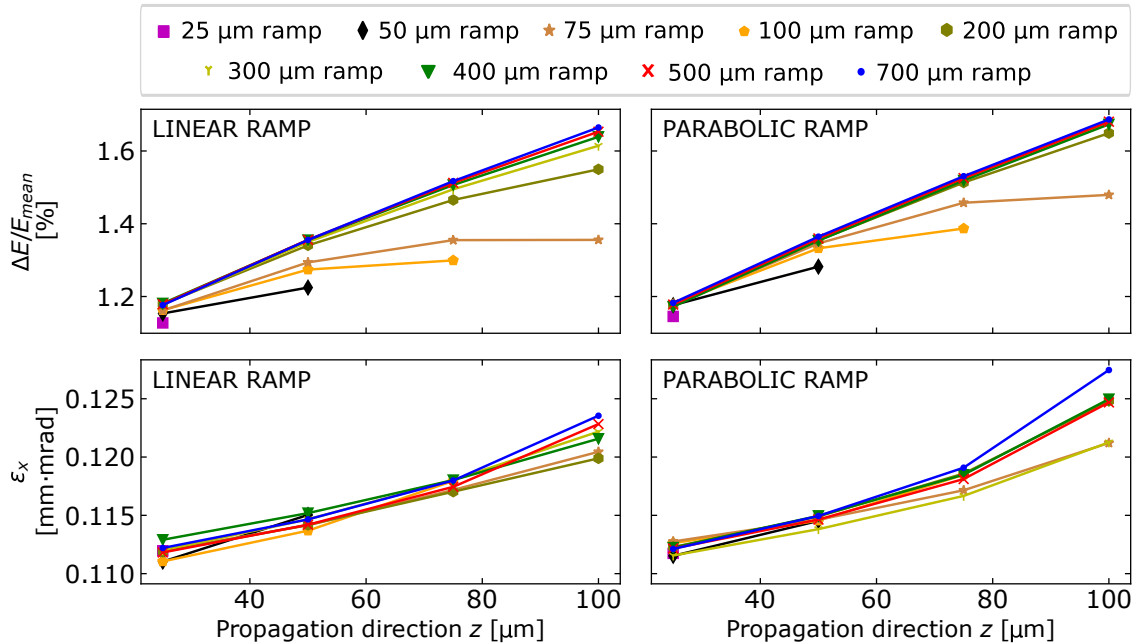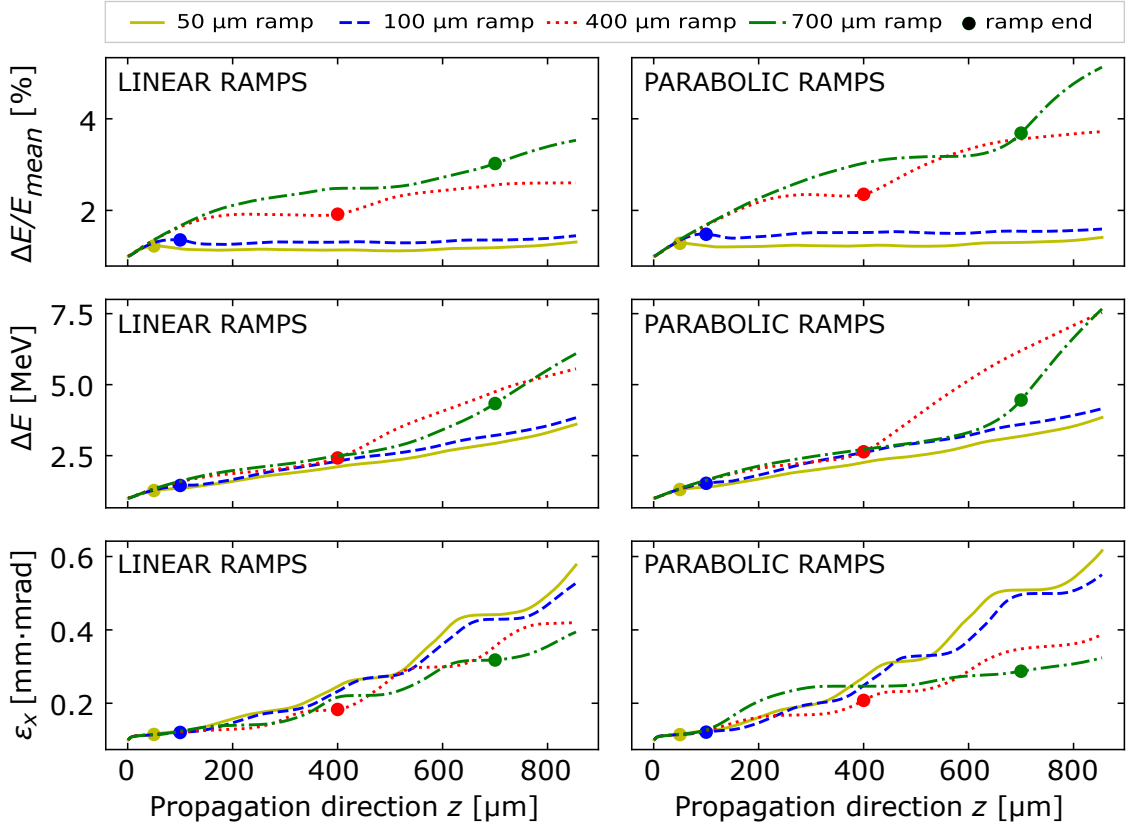
Figure 4.3: Evolution of the electron bunch relative energy spread $\Delta E/E_{mean}$ and transverse emittance ε_x for different ramp types during the first 100 µm of propagation is shown until each of the ramps respectively ends.

Even within these 50, 75, and 100 µm long ramps, those with the linear profile provide a smaller $\Delta E/E_{mean}$ of the electron bunch by ~ 0.07 % compared to those with the parabolic profile. The transverse emittance ε_x is overall very similar between linear and parabolic profiles, except that it is slightly elevated at $z \sim 100$ µm if parabolic profiles are used.

Looking further from the first 100 µm of the electron bunch propagation, the difference in parameters between linear and parabolic profiles is noticeable in the case of longer ramps. The same observation applies, with the exception of ΔE, to different lengths within the same (linear or parabolic) density profile. For instance, considering parabolic profiles, the individual values of the transverse emittance ε_x are more dispersed and elevated from $z \sim 200$ µm to 500 µm.

It is also useful to know how the bunch parameters develop after the transition to a uniform plasma density. It may happen that their value will be different after the transition. It is desirable for the electron bunch parameters not to change suddenly and, at best, to remain constant. Two short (50 µm, 100 µm) and two long (400 µm, 700 µm) plasma density ramps for each profile (linear and parabolic) were chosen, for which the evolution of the bunch parameters was monitored during the entire duration of the simulation. The results are shown in Figure 4.4.

Figure 4.4: Evolution of the electron bunch properties within the span of $T_{sim} \sim 3$ ps for linear and parabolic ramps of different lengths. The circle indicates the ramp end.

Figure 4.4 clearly shows that in the case of 2D simulations, short density ramps have the opposite effect on relative energy spread as longer ramps. Notably, a stabilization of $\Delta E/E_{mean}$ can be seen after the end of each short ramp, i.e., 50 µm and 100 µm. In contrast, for longer ramps, $\Delta E/E_{mean}$ increases after the end of the ramp. Emittance growth is similar for linear and parabolic ramps of the same length, being highest for the shortest ramps.

In Figure 4.5 the density profiles of the simulations with a 50 µm and 400 µm linear ramp were compared at simulation time $T_{sim} \sim 3$ ps. At this time, the wakefield is formed in both cases.
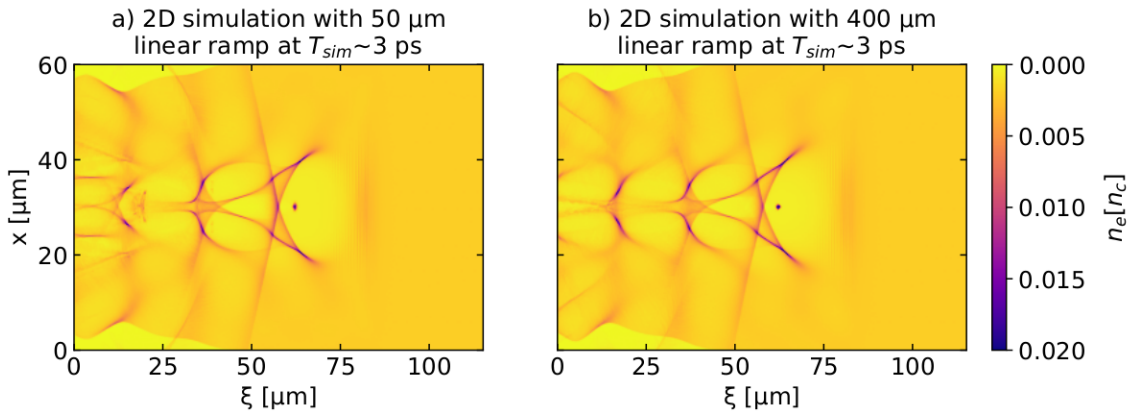
Figure 4.5: Plasma density profiles with the initial linear ramp of the length a) $L_r = 50$ µm and b) $L_r = 400$ µm at $T_{sim} \sim 3$ ps.

However, it should be noted that the longer the ramp, the slower the wakefield formation process. In other words, bunch capture in the bubble takes place at a greater distance from the beginning of the plasma. For example, Figure 4.6a) shows that in the case of a 50 μm ramp, the corresponding wakefield (i.e., its normalized longitudinal electric field E_z/E_0) is already formed at 50 μm, so it is already affecting the electron bunch. It is also clear that the longitudinal field of the wakefield related to the 400 μm ramp has a lower value at the same position. Furthermore, the claim of a slower formation of the wakefield in longer ramps is also supported by Figure 4.7a), in which the evolution of the electron bunch energy is depicted. Particularly as the electron bunch propagates in a 400 μm linear ramp, its energy until $z \sim 200$ μm remains constant or even slightly decreases. Only after the wakefield is formed does the bunch start to gain energy.
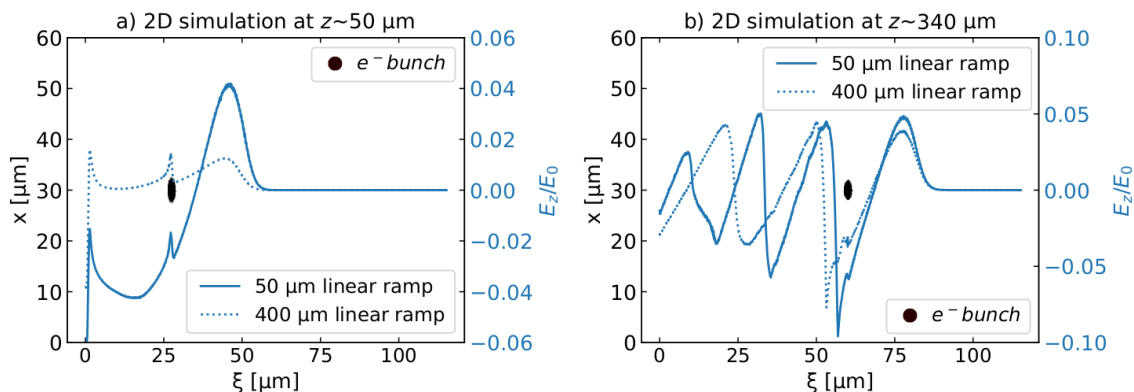

Figure 4.6: The structure of the wakefield normalized electric field E_z/E_0 in the longitudinal direction for $x = 30$ μm acting on the electron bunch positioned at a) $z \sim 50$ μm and b) $z \sim 340$ μm for both $L_r = 50$ μm (blue solid line) and $L_r = 400$ μm (blue dotted line) linear ramps. The corresponding electron bunches (black area) from each simulation overlap.

Not only is the formation of the wakefield slower in the case of longer ramps, but its shape is also different. Figure 4.5b) shows that in the case of a longer ramp, the density profile formed by the wakefield is slightly different compared to the one formed in the shorter ramp. Moreover, Figure 4.6b) shows that the electron bunch associated with 50 μm linear ramp is positioned closer to the left boundary (rear part) of the first bubble and the acting E_z/E_0 is larger. In general, the wakefield amplitudes are larger at these boundaries. Therefore, their influence is more significant. The further the electron bunch is from the bubble boundary (as in the case of a 400 μm ramp), the less it is influenced by the longitudinal forces of the wakefield. Note that the electron bunch in the simulation with the 50 μm ramp is located at the same position as in the simulation with the 400 μm ramp. For this reason, the color representation of the corresponding electron bunch was chosen by one color for both simulations.

Figure 4.6b) also indicates that in both cases, the corresponding E_z/E_0 acts almost uniformly on the whole electron bunch in the displayed position. It shows how the electron bunch itself affects this field, which is a characteristic feature of beam loading [131]. A closer look at this region in (Figure 4.7b)) shows that E_z/E_0 in the simulation with the 400 μm ramp slightly oscillates. This means that electrons within the bunch experience at this position of acceleration different longitudinal fields. It seems that at this position of observation (at $z \sim 340$ μm), these oscillations do not influence the energy of the electrons.
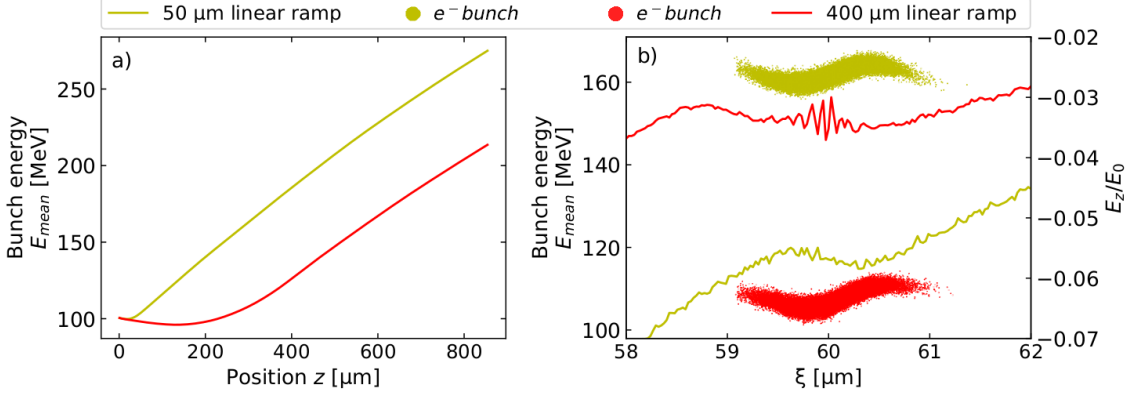
Figure 4.7: a) Evolution of the electron bunch energy E_{mean} within the span of $T_{sim} \sim 3$ ps in a 2D simulation in which a 50 μm (olive line) and 400 μm (red line) linear ramp was used. b) Zoomed area of the normalized longitudinal electric field E_z/E_0 structure (right axis) in the wakefield at $z \sim 340$ μm, in the case of 50 μm (olive line) and 400 μm (red line) linear ramps. The energy of the electron bunch (left axis) that propagates in the linear ramp with a specific length is marked with the corresponding color. Each dot represents one electron macro-particle of the bunch.

If the same observation is made at the end of the simulation (at $z \sim 900$ μm), then Figure 4.8a) shows that E_z/E_0 are basically the same. A closer look in Figure 4.8b) at the region of E_z/E_0 acting on both electron bunches at $z \sim 900$ μm shows that those distinct oscillations shown in Figure 4.7b) disappeared. Nevertheless, Figure 4.8b) depicts that their influence was strong enough to cause a disturbance in the mean energy E_{mean} of individual electrons within the bunch propagating in the 400 μm linear ramp.
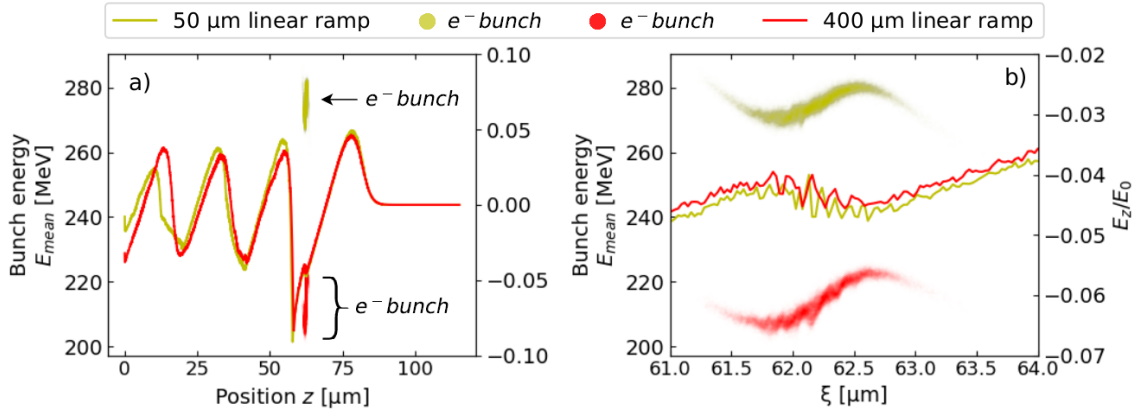
**Figure 4.8:** a) The structure of the wakefield normalized electric field E_z/E_0 in the longitudinal direction for $x = 30$ μm acting on the electron bunch at $z \sim 900$ μm propagating in 50 μm (olive line) and 400 μm (red line) linear ramps. The electron bunch (left axis) that propagates in the linear ramp with a specific length is marked with the corresponding color. b) Zoomed area of E_z/E_0 structure (right axis) in the wakefield at $z \sim 900$ μm in the case if 50 μm (olive line) and 400 μm (red line) linear ramps are used. The electron bunch (left axis) that propagates in the linear ramp with a specific length is marked with the corresponding color.

These observations all together can explain the slight but steady increase in electron bunch parameters in the longer ramps before and after their end. For example, even though Figure 4.4 shows that ΔE increases during the entire simulation for both shorter and longer ramps, the energy gain is smaller when longer ramps are used.

This essentially means that the denominator in $\Delta E/E_{mean}$ is smaller and thus its final value is significantly larger for longer ramps.

The same argument applies when linear and parabolic ramps are compared. However, due to the smaller absolute values of the density in the parabolic profile (compared to the linear profile), the electron density is distributed differently. Particularly, the electron bunch travels in less dense plasma at the beginning compared to the linear ramp with the same length. Formation of the wakefield thus takes a longer time and the electron bunch will essentially gain less energy, as can be seen on Figure 4.9. This reflects on the rest of the bunch parameters, as mentioned above.
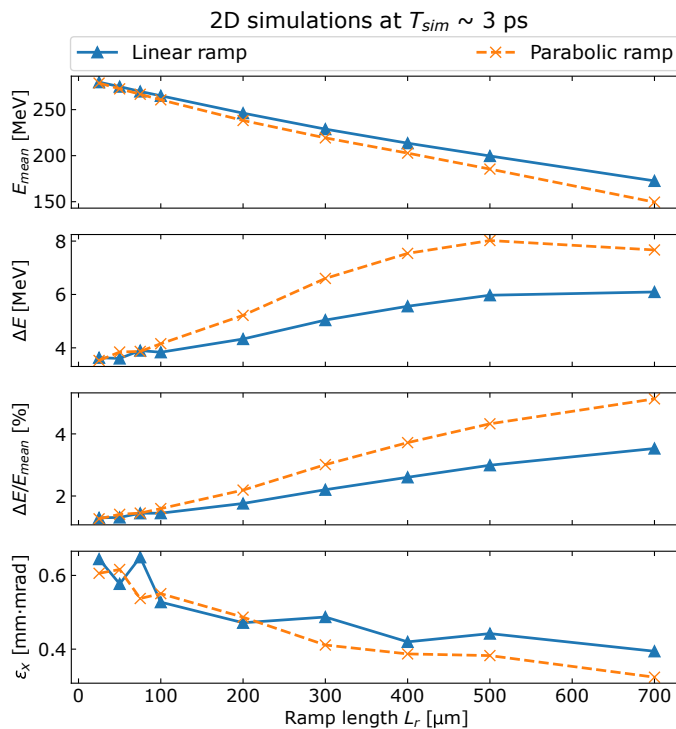

Figure 4.9: Final values of the electron bunch parameters at the end of the 2D simulation at $T_{sim} \sim 3$ ps; from the top to the bottom: mean energy of the electron bunch E_{mean}, energy spread ΔE, relative energy spread $\Delta E/E_{mean}$, and transverse emittance ε_x. The values are shown for simulations with different ramp lengths L_r.

4.3 Results of 3D simulations

Due to the differences between the wakefield properties in 2D and 3D particle-in-cell simulations (as mentioned above), this work also includes the results from the latter. In this regard, 2D simulations serve only to provide initial assumptions, which will be verified based on the results of 3D simulations. Based on the 3D simulations, a more accurate conclusion can be established.

Similar to the previous case in Figure 4.2, it can be assumed from Figure 4.10 that the examined properties of the bunch do not significantly depend on the length and profile of the ramps during the first 100 μm of the propagation.
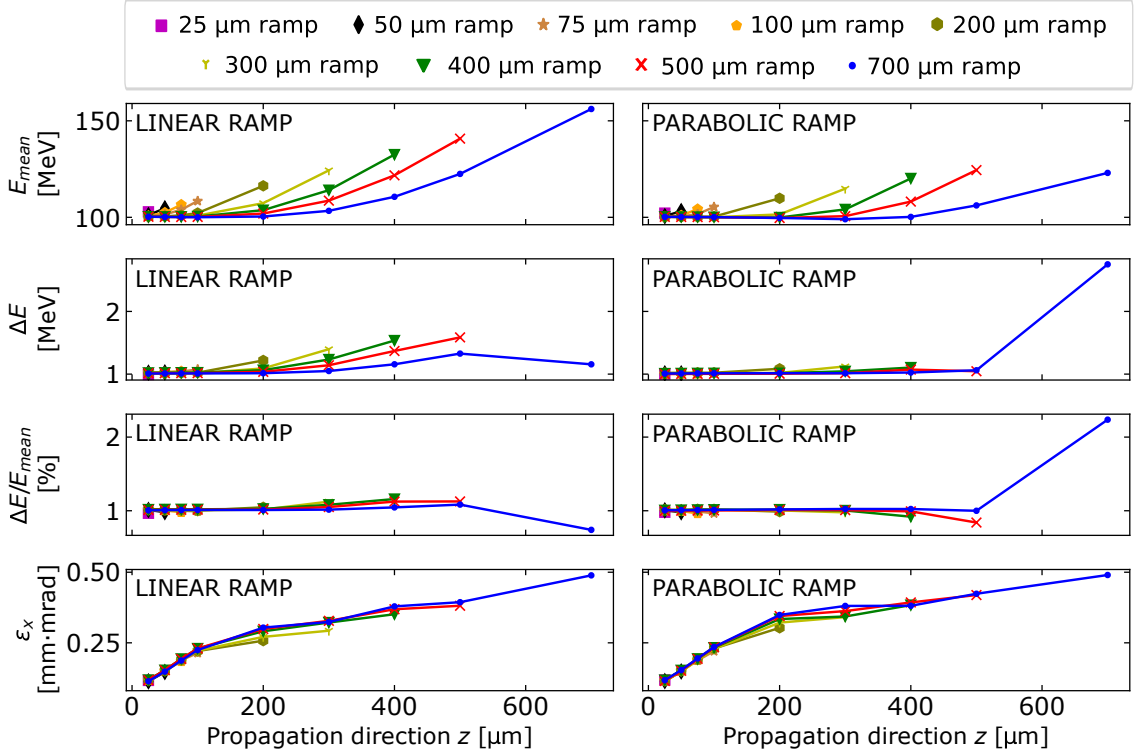
Figure 4.10: Evolution of the beam energy E_{mean}, energy spread ΔE, relative energy spread $\Delta E/E_{mean}$, and transverse emittance ε_x for different ramp lengths and profiles is shown until each of the ramps respectively ends.

A closer observation of this acceleration stage was also made in the case of 3D simulations, and the results in Figure 4.11 show that the transverse emittance ε_x increases equally, not only for the two ramp profiles but also for different lengths.
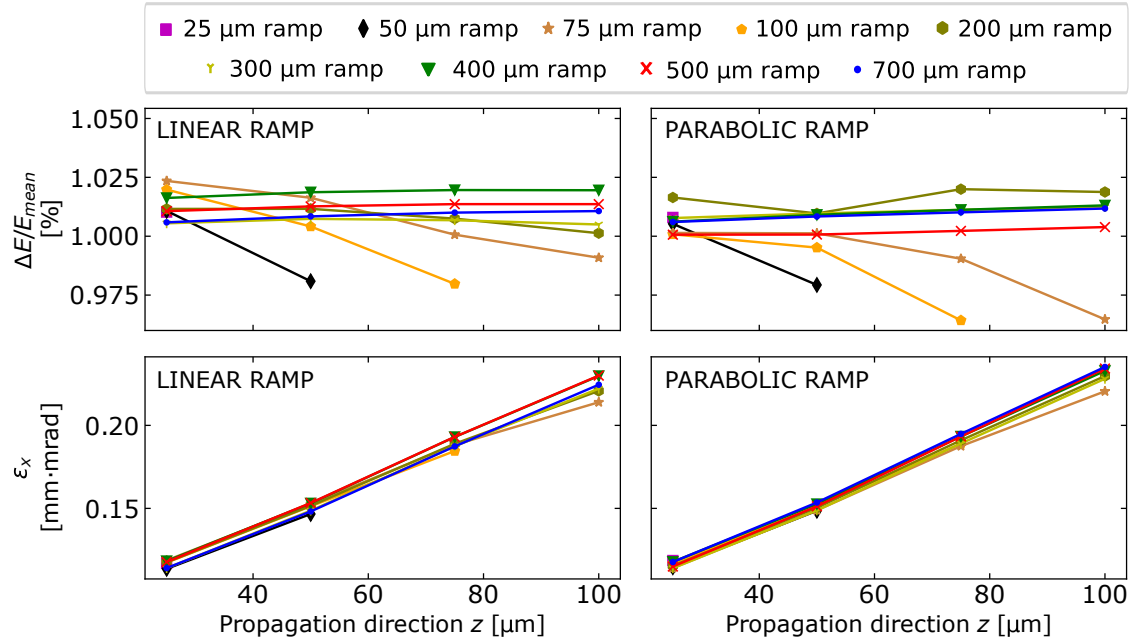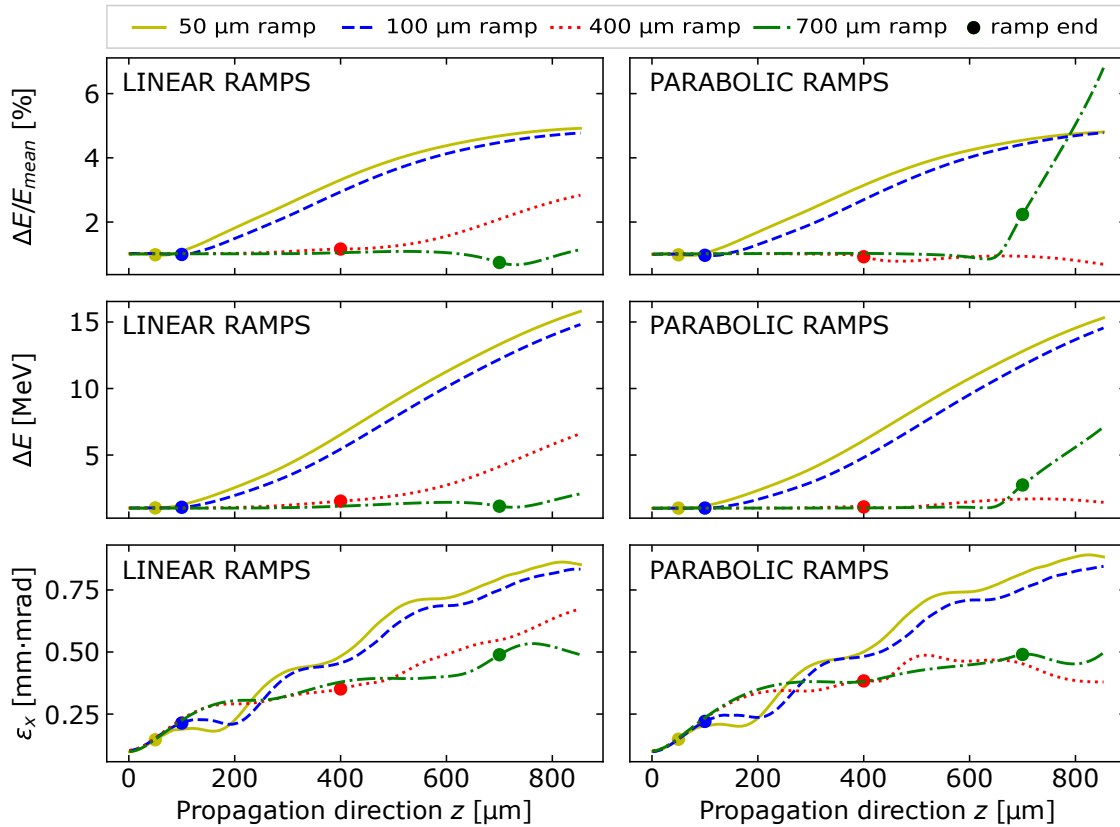

Figure 4.11: Evolution of the electron bunch relative energy spread $\Delta E/E_{mean}$ and transverse emittance ε_x for different ramp types during the first 100 μm of propagation is shown until each of the ramps respectively ends.

It seems that shorter ramps are able to provide the decrease of $\Delta E/E_{mean}$ of the
bunch during the 100 μm of the propagation. This can be due to the fact that in
shorter ramps, the wakefield forms earlier. Owing to this, the wakefield is able to
focus the bunch sooner into a smaller size, which affects $\Delta E/E_{mean}$. On the other
hand, longer parabolic ramps are better at preserving the initial value of $\Delta E/E_{mean}$,
but the differences between them and their linear equivalents are essentially negligi-
ble. The most interesting observation in Figure 4.11 is that the energy spread of the
bunch propagating in the 400 μm parabolic ramp almost did not change compared
to its initial value.

Based on Figure 4.10, energy spread ΔE and relative energy spread $\Delta E/E_{mean}$ are
mostly constant when the parabolic profiles are used, regardless of their length.
Moreover, in the case of the 400 μm and 500 μm parabolic ramp, the relative energy
spread $\Delta E/E_{mean}$ even decreases compared to the initial value of 1 %. The biggest
difference between linear and parabolic ramps in observed transverse emittance ε_x
can be seen at $z \sim 200$ μm and 300 μm. At these positions, the transverse emittance
relative to the linear ramps is on average lower by approximately 0.01 mm·mrad and
0.02 mm·mrad, respectively.

However, a rapid increase in ΔE and $\Delta E/E_{mean}$ is observed when a 700 μm parabolic
ramp is used. In order to explain this phenomenon, the time evolution of the pa-
rameters of the corresponding electron bunch as well as of the other 3 bunches
propagating in 50 μm, 100 μm, and 400 μm ramps were compared. The results are
shown in Figure 4.12. It can be seen that the increase in ΔE and $\Delta E/E_{mean}$ of the
electron bunch propagating in the 700 μm parabolic ramp started before its end.

Figure 4.12: Evolution of the electron bunch properties within the span of $T_{sim} \sim 3$ ps for linear
and parabolic ramps of different lengths in 3D PIC simulations. The circle indicates the ramp end.
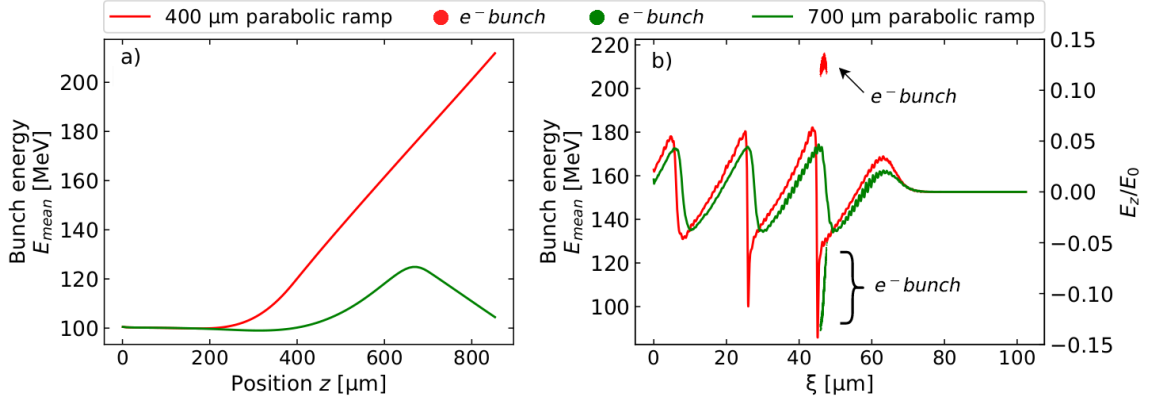
Figure 4.13: a) Evolution of the electron bunch mean energy E_{mean} within the span of $T_{sim} \sim 3$ ps in a 3D simulation in which a 400 µm (red line) and 700 µm (green line) parabolic ramp was used. b) Structure of the normalized longitudinal electric field E_z/E_0 (right axis) in the wakefield at $z \sim 900$ µm in the case if 400 µm (red line) and 700 µm (green line) parabolic ramps are used. The energy of the electron bunch (left axis) that propagates in the linear ramp with a specific length is marked with the corresponding color. Each dot represents one electron macro-particle of the bunch.

Nevertheless, by comparing the energy evolution between the electron bunches in the 400 µm and 700 µm parabolic ramps (Figure 4.13a)) as well as the structure of the corresponding E_z/E_0 at the end of the simulation (Figure 4.13b)), the explanation can be found. The rapid change in the parameters was caused by electron bunch slippage from the back of the bubble.

As Figure 4.13a) shows, the electron bunch propagating in a 700 µm parabolic ramp began to accelerate only at $z \sim 400$ µm, and even before that, it lost some of its initial energy. Furthermore, as mentioned in the previous subsection, the formation of the wakefield (strong enough to accelerate the electron bunch) in longer density ramps takes place later in the plasma compared to the shorter ramps. As a result, the position of the electron bunch changed relatively to the bubble position due to the different position of the bubble rear part, as the wakefield was formed in a different manner. Consequently, as Figure 4.13b) indicates, the electron bunch (green stretched mark) has passed behind the boundary of the first bubble where its properties rapidly deteriorated.

Analogous to the results from 2D simulations, also in the case of 3D simulations, the values of the electron bunch parameters were examined at the end of the simulation, i.e., at $T_{sim} \sim 3$ ps (Figure 4.14).
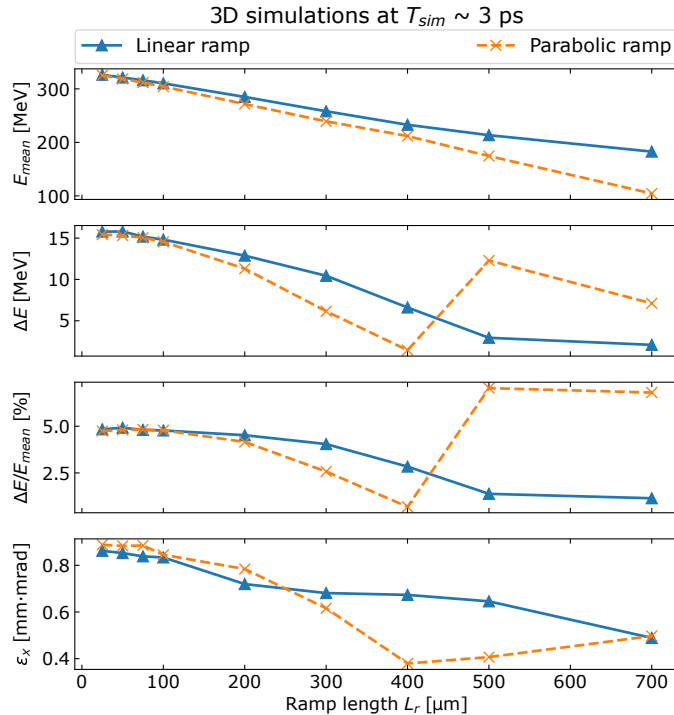
Figure 4.14: Final values of the electron bunch parameters at the end of the 3D simulation at $T_{sim} \sim 3$ ps; from the top to the bottom: mean energy of the electron bunch E_{mean}, energy spread ΔE, relative energy spread $\Delta E/E_{mean}$, and transverse emittance ε_x. The values are shown for simulations with different ramp lengths L_r.

As mentioned earlier, the relative energy spread $\Delta E/E_{mean}$ of the electron bunch propagating in a 500 µm parabolic ramp (based on Figure 4.10) was smaller than its initial value at the end of the ramp, thus indicating a very promising further development of its parameters. However, with regard to this case, Figure 4.14 shows sudden increase in energy spread ΔE and also $\Delta E/E_{mean}$ at the end of the simulation. For this reason, the time evolution of its parameters was compared with the evolution of the parameters of the bunch propagating in the 400 µm parabolic ramp, which showed similar and quantitatively equal values of $\Delta E/E_{mean}$, ΔE, and transverse emittance ε_x at $z \sim 400$ and 500 µm. Figure 4.15 thus shows the exact position where the undesirable increase occurred.

Particularly, from Figure 4.15 it is clear that relative energy spread $\Delta E/E_{mean}$ began to increase at $z \sim 560$ µm, until the end of the simulation. As in the previous case with 700 µm parabolic ramp, it is possible to assume that at $z \sim 560$ µm the electron bunch was positioned too close to the boundary of the first bubble, where E_z/E_0 is strongly non-linear, which caused the degradation of its parameters. Figure 4.16b) confirms this assumption. Figure 4.16c) indicates that this electron bunch was placed at the rear boundary of the bubble, in contrast to 400 µm ramp, where the accelerating structure was well-formed in the bunch position. Ultimately, this event led to the deterioration of the bunch's parameters at the end of the simulation.
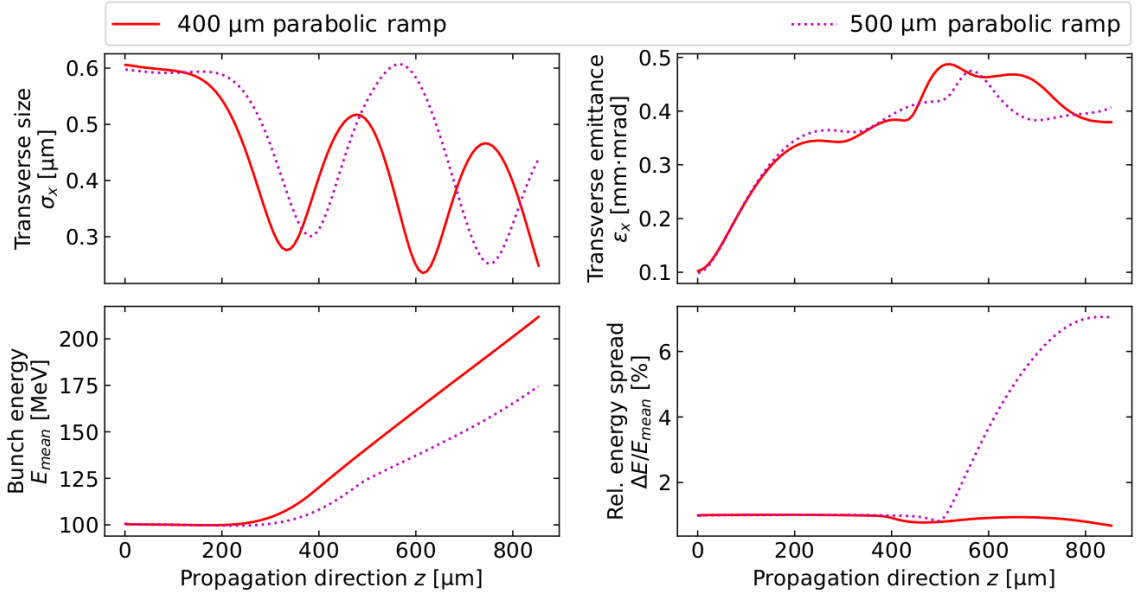
Figure 4.15: Evolution of the electron bunch properties within the span of $T_{sim} \sim 3$ ps propagating in a 400 µm (red solid line) and 500 µm (magenta dotted line) parabolic ramps.
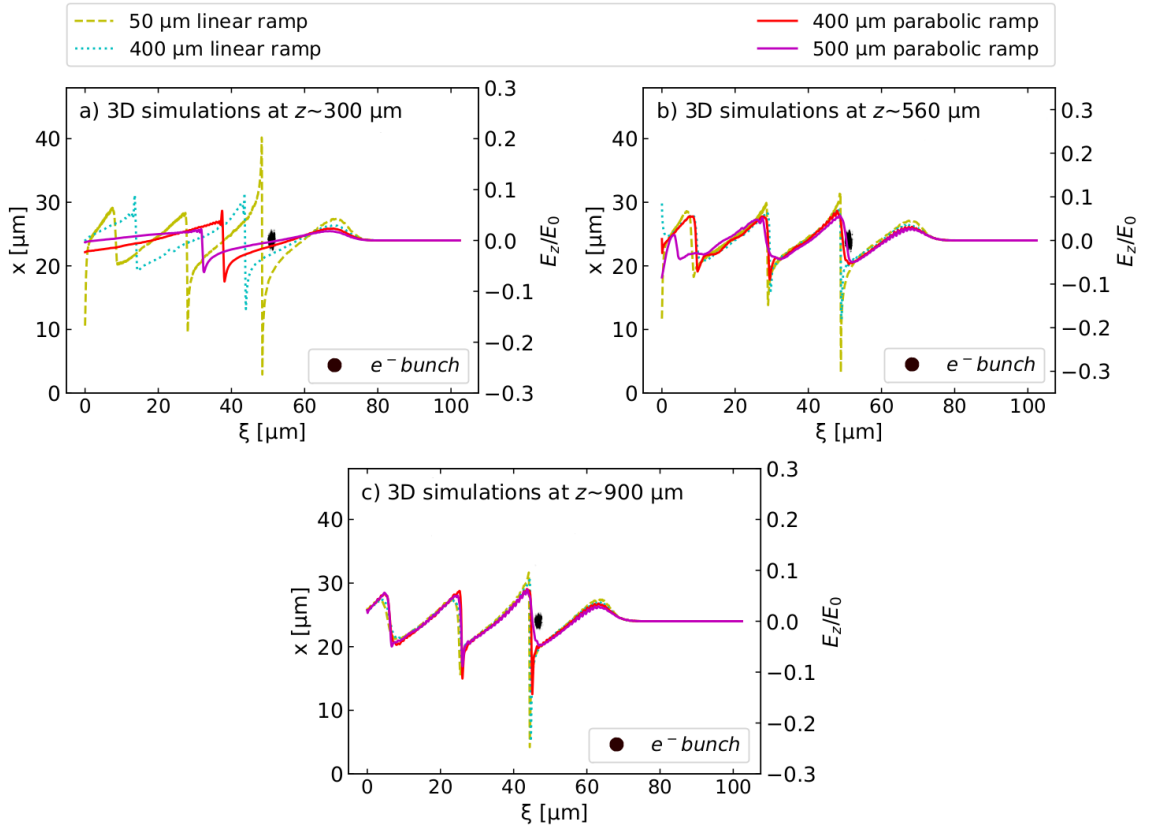
Figure 4.16: The structure of the wakefield normalized electric field E_z/E_0 in the longitudinal direction for $x = 30$ µm (the laser propagation axis) acting on the electron bunch at a) $z \sim 300$ µm, b) $z \sim 560$ µm, and c) $z \sim 900$ µm for two $L_r = 50$ µm (olive dashed line), $L_r = 400$ µm (cyan dotted line) linear and two $L_r = 400$ µm (red solid line), $L_r = 500$ µm (magenta solid line) parabolic ramps. The corresponding electron bunches (black area) overlap. For this reason, they are marked with the same color.

In contrast to the 2D simulations, in the 3D simulations, ΔE and $\Delta E/E_{mean}$ significantly increases after the ramp for short ramps (50 μm and 100 μm). Generally, longer ramps show better results. Not only are they able to maintain ΔE and $\Delta E/E_{mean}$ of the electron bunch throughout the entire simulation, but ε_x is also noticeably lower. The problem with the 500 μm parabolic ramp was already discussed, however, Figure 4.16b) also shows why ΔE and $\Delta E/E_{mean}$ of the electron bunch propagating in 400 μm linear ramp increases at $z \sim 560$ μm. From the position of the bunch in the bubble, it can be seen how its rear part is affected by a more non-linear field E_z/E_0 than the front part. Figure 4.16a) shows the direct reason why bunch propagation in longer ramps leads to better results. In both cases, the bunch travelling in the 400 μm and 500 μm parabolic ramps is affected by an almost uniform E_z/E_0 throughout its length.

As discussed earlier, due to the different formation of the wakefield in longer ramps, the electron bunch can travel behind the bubble. Because of this, two additional 3D simulations were performed in which 400 and 500 μm parabolic ramps were used with a different initial distance between the bunch and the laser than $s_{3D} = 16.85$ μm. Figure 4.17 shows that even finer tuning of s_{3D} would be needed, but in the case of the 500 μm parabolic ramp with $s_{3D} = 14.85$ μm, it was possible to significantly reduce $\Delta E/E_{mean}$.
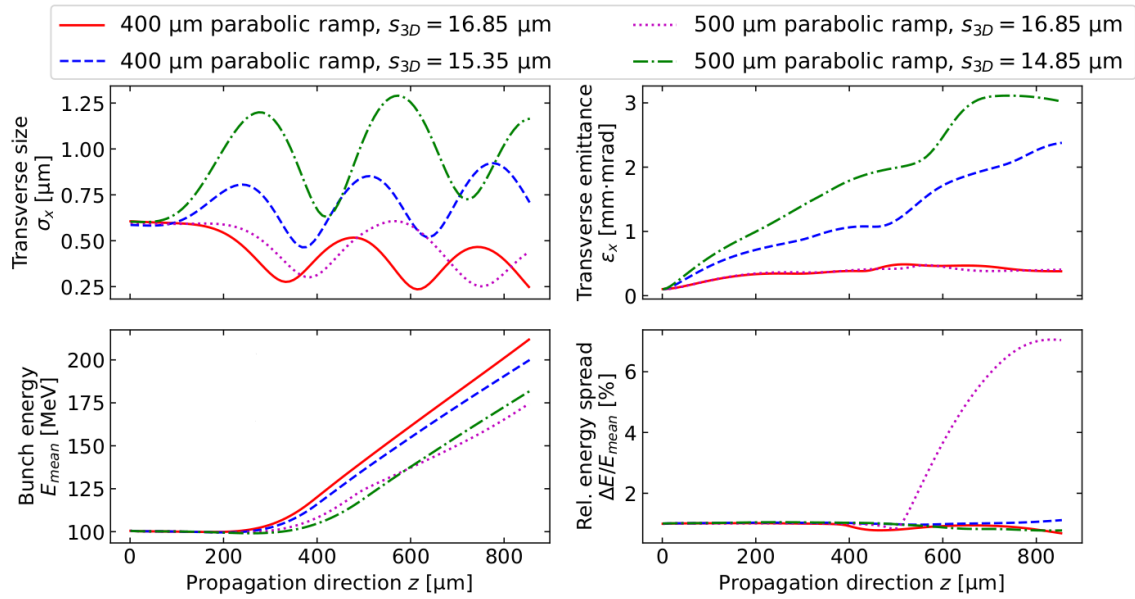
Figure 4.17: Evolution of the electron bunch properties within the span of $T_{sim} \sim 3$ ps in 3D PIC simulations for parabolic ramps of different lengths and different distances s_{3D} between the electron bunch and laser pulse.

Based on the obtained results, it has been shown that the use of a 400 μm parabolic ramp (in relation to the rest of the parameters in Table 4.1 and Figure 4.1) provides the best conditions for the preservation of the electron bunch parameters.

Discussion and conclusion

Laser wakefield acceleration (LWFA) represents an innovative method of accelerating electron beams in plasma, using electric fields several orders of magnitude higher than those available in conventional accelerators. As a result, it is possible to significantly reduce the length of the acceleration. However, experiments demonstrating laser wakefield acceleration often suffer from a fundamental lack of control or large shot-to-shot fluctuations. This is because, in most of the current injection schemes, the injection of electrons and their subsequent acceleration are intrinsically dependent on each other. These schemes are based on non-linear dynamics, in which electrons are injected from the plasma background itself. This can lead to a situation in which the properties of injected electrons acquire undesirable values even before they are subjected to acceleration. This is also why the idea of injecting from a separate, external accelerator is currently growing in popularity, so that the injection can be controlled better [4]. At the same time, it is possible to take advantage of the fact that electrons produced from an external source have well-known and, in this sense, "fixed" parameters.

However, external injection requires exquisite alignment and timing between the electron bunch and the laser pulse. It also requires vacuum isolation between the conventional RF accelerator and the LWFA stage. In this finite transition region (or rather, density ramp), the plasma wavelength changes gradually, which means that the injected electrons can be affected by the altering wakefield. Nevertheless, it has been demonstrated that the emittance growth or energy spread can be mitigated using long (mm-scale) density ramps [70]. The aim of this work was to examine if short (tens-of-micron scale) plasma density ramps of different lengths and different profiles (linear or convex parabolic) play a significant role in the injection of the electron bunch and, also, how much it affects its final parameters.

Based on 2D simulations, which were carried out first because they are computationally less demanding, it was found that for short ramps (25 - 100 μm), there is no significant difference in the final bunch parameters. Also, the profile type (linear or parabolic) did not influence the result. Additionally, based on Figure 4.6b) and Figure 4.7b), it was shown that a different normalized longitudinal electric field E_z/E_0 acts on the electron bunch during the transition through the ramp and even shortly after the transition to the uniform density if short (< 100 μm) or longer (> 100 μm) ramps are used. In the case of shorter ramps, the resulting field preserves the initial properties of the bunch with better efficiency. Nevertheless, as can be seen in Figure 4.8 (the continuation of Figure 4.6), E_z/E_0 have the same shape and size at the end of the simulation. However, the bunch (red colored area), which was exposed

to a field of higher non-linearity of the 400 µm ramp during acceleration, acquired a larger energy spread ΔE and relative energy spread $\Delta E/E_{mean}$.

Due to the different equations for the wakefield and the bubble's boundary used in the 2D and 3D geometry [130] as well as the different focusing of the laser pulse [129], the generated wakefield has a 2D elongated shape in the longitudinal direction and a round shape in the 3D geometry. For this reason, 3D simulations with the same parameters (except for the distance between the laser and the electron beam, which had to be shortened by 1 µm based on the test simulations) were also performed. It was confirmed that the length and profile of plasma density ramps do not play a significant role on electron bunch parameters during the first 100 µm of the propagation. However, in contrast to the 2D simulations, energy spread ΔE and relative energy spread $\Delta E/E_{mean}$ significantly increase after the transition to uniform density if short ramps (50 and 100 µm) are used.

On the other hand, long parabolic ramps, especially the 400 µm ramp, show promising and stable results. Figure 4.16a) and Figure 4.16c) show that E_z/E_0 of the wakefield created in longer ramps has a different shape. This field also depends on the type of the profile. The explanation of why these fields have different shapes is rather simple. The use of longer ramps, i.e., a smaller initial plasma density, as well as the use of parabolic profile, causes the bubble formation to take place at a greater distance from the start of the simulation. In other words, the laser pulse must travel a longer distance in a less dense plasma to "pick up" enough plasma electrons to form a bubble wakefield. From the beginning, a less non-linear acceleration field is created in the wakefield, which acts uniformly on the electron bunch and thus does not worsen its parameters. However, as the laser and the wakefield travel further into the plasma, more and more plasma electrons flow around the bubble and concentrate in the rear part, which creates a non-linear, sawtooth-like negative gradient. In this sense, longer density ramps as well as the use of a parabolic density profile offer a more adiabatic process of wakefield formation than plasma in shorter ramps, where the sharp negative gradient is already present at the very beginning of the simulation. It has been already discussed how these highly non-linear gradients cannot be compensated using positive chirp by Lu et al. [36]. Therefore, it is necessary to ensure that these gradients are avoided at the very beginning of injecting the beam into the wakefield.

At the end of the fourth chapter, it was pointed out that, due to a different formation of the wakefield that can occur while the wakefield is forming in longer ramps, the initial distance between the bunch and the bubble rear part can change. Because of this, two additional 3D simulations were performed, in which 400 and 500 µm parabolic ramps were used with a different distance between the bunch and the laser pulse than the one originally assumed in this work ($s_{3D} = 16.85$ µm). However, Figure 4.17 shows that even finer tuning of s_{3D} is needed, and the 400 µm parabolic ramp with $s_{3D} = 16.85$ µm still provides the best results among the examined cases.

It is important to note that, in order to be able to correctly decide whether longer ramps, especially those with a parabolic profile, are the most effective in preserving the initial values of the bunch parameters, it is necessary to carry out longer simulations up to the dephasing phase. It is possible that in later acceleration stages,

the bunch parameters evolve in a different manner than anticipated here based on the earlier stages. This work focused mainly on the effect of such ramps during the injection and the first ~ 1 mm of acceleration, since the deterioration of the bunch's parameters already at this initial stage could be more difficult to compensate later.

In conclusion, using longer parabolic plasma density ramps for effective capture of the electron bunch and its acceleration, even at the cost of less achievable energy (in comparison with short linear ramps) is recommended. For the parameters that were used in this work, the 400 μm convex parabolic ramp is especially beneficial since it provided the lowest values of energy spread ΔE, relative energy spread $\Delta E/E_{mean}$, and transverse emittance ε_x.

Bibliography

1. BRÜMMER, T.; DEBUS, A.; PAUSCH, R.; OSTERHOFF, J.; GRÜNER, F. Design study for a compact laser-driven source for medical x-ray fluorescence imaging. *Phys. Rev. Accel. Beams.* 2020, roč. 23, p. 031601. Available from DOI: `10.1103/PhysRevAccelBeams.23.031601`.

2. SIMONS, J. P.; HUTCHINSONS, M. H. R.; DITMIRE, T.; SPRINGATE, E.; TISCH, J. W. G.; SHAO, Y. L.; MASON, M. B.; HAY, N.; MARANGOS, J. P. High-intensity lasers: interactions with atoms, molecules and clusters. *Philosophical Transactions of the Royal Society of London. Series A: Mathematical, Physical and Engineering Sciences.* 1998, roč. 356, č. 1736, pp. 297–315. Available from DOI: `10.1098/rsta.1998.0166`.

3. FLOETTMANN, K. Some basic features of the beam emittance. *Phys. Rev. ST Accel. Beams.* 2003, roč. 6, p. 034202. Available from DOI: `10.1103/PhysRevSTAB.6.034202`.

4. GREBENYUK, J.; MEHRLING, T.; TSUNG, F. S.; FLOETTMAN, K.; OSTERHOFF, J. Simulations of laser-wakefield acceleration with external electron-bunch injection for REGAE experiments at DESY. *AIP Conference Proceedings.* 2012, roč. 1507, č. 1, pp. 688–692. Available from DOI: `10.1063/1.4773781`.

5. MEHRLING, T.; GREBENYUK, J.; TSUNG, F. S.; FLOETTMANN, K.; OSTERHOFF, J. Transverse emittance growth in staged laser-wakefield acceleration. *Phys. Rev. ST Accel. Beams.* 2012, roč. 15, p. 111303. Available from DOI: `10.1103/PhysRevSTAB.15.111303`.

6. WEIKUM, M.; ASSMANN, R.; DORDA, U.; P., Ferran; HEINEMANN, T. et al. Improved Electron Beam Quality from External Injection in Laser-Driven Plasma Acceleration at SINBAD. 2017. Available from DOI: `10.18429/JACoW-IPAC2017-TUPIK013`.

7. DEROUILLAT, J.; BECK, A.; PÉREZ, F.; VINCI, T.; CHIARAMELLO, M.; GRASSI, A.; FLÉ, M.; BOUCHARD, G.; PLOTNIKOV, I.; AUNAI, N.; DARGENT, J.; RICONDA, C.; GRECH, M. Smilei : A collaborative, open-source, multi-purpose particle-in-cell code for plasma simulation. *Computer Physics Communications.* 2018, roč. 222, pp. 351–373. ISSN 0010-4655. Available from DOI: `https://doi.org/10.1016/j.cpc.2017.09.024`.

8. KRANE, K. S. Introductory nuclear physics. 1988. Available also from: `https://cds.cern.ch/record/359790`.

9. AKRE, R.; DOWELL, D.; EMMA, P.; FRISCH, J.; GILEVICH, S.; HAYS, G.; HERING, Ph.; IVERSON, R.; LIMBORG-DEPREY, C.; LOOS, H.; MI-AHNAHRI, A.; SCHMERGE, J.; TURNER, J.; WELCH, J.; WHITE, W.; WU, J. Commissioning the Linac Coherent Light Source injector. *Phys. Rev. ST Accel. Beams.* 2008, roč. 11, p. 030703. Available from DOI: `10.1103/PhysRevSTAB.11.030703`.

10. ESAREY, E.; SPRANGLE, P.; KRALL, J.; TING, A. Overview of plasma-based accelerator concepts. *IEEE Transactions on Plasma Science.* 1996, roč. 24, č. 2, pp. 252–288. Available from DOI: `10.1109/27.509991`.

11. TAJIMA, T.; DAWSON, J. M. Laser Electron Accelerator. *Phys. Rev. Lett.* 1979, roč. 43, pp. 267–270. Available from DOI: `10.1103/PhysRevLett.43.267`.

12. NAKAJIMA, K. Compact X-ray sources: Towards a table-top free-electron laser. *Nature Physics.* 2008, roč. 4, pp. 92–93. Available from DOI: `10.1038/nphys846`.

13. WIEL, M. J. van der; LUITEN, O. J.; BRUSSAARD, G. J. H.; GEER, S. B. van der; URBANUS, W. H.; DIJK, W. van; OUDHEUSDEN, Th. van. Laser wakefield acceleration: the injection issue. Overview and latest results. *Philosophical Transactions of the Royal Society A: Mathematical, Physical and Engineering Sciences.* 2006, roč. 364, č. 1840, pp. 679–687. Available from DOI: `10.1098/rsta.2005.1731`.

14. GIBBON, P. Introduction to Plasma Physics. 2016, p. 16. Available from DOI: `10.5170/CERN-2016-001.51`.

15. TONKS, L.; LANGMUIR, I. Oscillations in Ionized Gases. *Phys. Rev.* 1929, roč. 33, pp. 195–210. Available from DOI: `10.1103/PhysRev.33.195`.

16. YOON, Jin Woo; KIM, Yeong Gyu; AL., Il Woo Choi et. Realization of laser intensity over $10^{23}\mathrm{W/cm^2}$. *Optica.* 2021, roč. 8, č. 5, pp. 630–635. Available from DOI: `10.1364/OPTICA.420520`.

17. SPRANGLE, P.; HAFIZI, B. High-power, high-intensity laser propagation and interactions. *Physics of Plasmas.* 2014, roč. 21, č. 5, p. 055402. Available from DOI: `10.1063/1.4878356`.

18. HAUS, H. A. Mode-locking of lasers. *IEEE Journal of Selected Topics in Quantum Electronics.* 2000, roč. 6, č. 6, pp. 1173–1185. Available from DOI: `10.1109/2944.902165`.

19. STRICKLAND, D.; MOUROU, G. Compression of Amplified Chirped Optical Pulses. *Optics Communications.* 1985, roč. 55, č. 6, pp. 447–449. ISSN 0030-4018. Available from DOI: `10.1016/0030-4018(85)90151-8`.

20. PASCHOTTA, R. *Field Guide to Lasers.* Society of Photo Optical, 2008. Field Guide Series. ISBN 9780819469618. Available also from: `https://books.google.sk/books?id=JPfUwAEACAAJ`.

21. MORA, P.; ANTONSEN Jr., T. M. Kinetic modeling of intense, short laser pulses propagating in tenuous plasmas. *Physics of Plasmas.* 1997, roč. 4, č. 1, pp. 217–229. Available from DOI: `10.1063/1.872134`.

22. CORNER, L. *Introduction to Laser Physics.* Proceedings of the 2019 CERN – Accelerator – School course on High Gradient Wakefield Accelerators, 2020.

23. ESAREY, E.; SCHROEDER, C. B.; LEEMANS, W. P. Physics of laser-driven plasma-based electron accelerators. *Rev. Mod. Phys.* 2009, roč. 81, pp. 1229–1285. Available from DOI: `10.1103/RevModPhys.81.1229`.

24. LEEMANS, W. P.; SIDERS, C. W.; ESAREY, E.; ANDREEV, N. E.; SHVETS, G.; MORI, W. B. Plasma guiding and wakefield generation for second-generation experiments. *IEEE Transactions on Plasma Science.* 1996, roč. 24, č. 2, pp. 331–342. Available from DOI: `10.1109/27.509997`.

25. CHEN, F. F. *Introduction to Plasma Physics.* Springer US, 2012. ISBN 9781475-704594.

26. FAURE, J.; GLINEC, Y.; PUKHOV, A.; KISELEV, S.; GORDIENKO, S.; LEFEBVRE, E.; ROUSSEAU, J. P.; BURGY, F.; MALKA, V. A laser-plasma accelerator producing monoenergetic electron beams. *Nature.* 2004, roč. 431, pp. 541–4. Available from DOI: `10.1038/nature02963`.

27. GEDDES, C.; TOTH, C.; TILBORG, J.; ESAREY, E.; SCHROEDER, C.; BRUHWILER, D.; NIETER, Ch.; CARY, J.; LEEMANS, W. High-quality electron beams from a laser wakefield accelerator using plasma-channel guiding. *Nature.* 2004, roč. 431, pp. 538–41. Available from DOI: `10.1038/nature02900`.

28. MANGLES, S.; MURPHY, Ch.; NAJMUDIN, Z.; THOMAS, A.; COLLIER, J.; DANGOR, A.; DIVALL, E.; FOSTER, P.; GALLACHER, J.; HOOKER, Ch.; JAROSZYNSKI, D.; LANGLEY, A.; MORI, W.; NORREYS, P.; TSUNG, F.; VISKUP, R.; WALTON, B.; KRUSHELNICK, K. Monoenergetic beams of relativistic electrons from intense laser-plasma interactions. *Nature.* 2004, roč. 431, pp. 535–8. Available from DOI: `10.1038/nature02939`.

29. PSIKAL, J.; TIKHONCHUK, V. T.; LIMPOUCH, J.; ANDREEV, A. A.; BRANTOV, A. V. Ion acceleration by femtosecond laser pulses in small multispecies targets. *Physics of Plasmas.* 2008, roč. 15, č. 5, p. 053102. Available from DOI: `10.1063/1.2913264`.

30. BOOT, H. A. H; HARVIE, R. B. R. S. Charged Particles in a Non-uniform Radio-frequency Field. *Nature.* 1957, roč. 180, pp. 1187–1187.

31. JOSHI, Ch. Laser-Driven Plasma Accelerators Operating in the Self-Guided, Blowout Regime. *IEEE Transactions on Plasma Science.* 2017, roč. PP(99), pp. 1–13. Available from DOI: `10.1109/TPS.2017.2769455`.

32. MANGLES, S. P. D.; MURPHY, C. D.; NAJMUDIN, Z.; THOMAS, A. G. R.; COLLIER, J. L.; DANGOR, A. E.; DIVALL, E. J.; FOSTER, P. S.; GALLACHER, J. G.; HOOKER, C. J.; JAROSZYNSKI, D. A.; LANGLEY, A. J.; MORI, W. B.; NORREYS, P. A.; TSUNG, F. S.; VISKUP, R.; WALTON, B. R.; KRUSHELNICK, K. Monoenergetic beams of relativistic electrons from intense laser–plasma interactions. *Nature.* 2004, roč. 431, č. 7008, pp. 535–/538. ISSN 1476-4687. Available from DOI: `10.1038/nature02939`.

33. GORBUNOV, L. M.; KIRSANOV, V. I. The excitation of plasma waves by an electromagnetic wave packet. *Zhurnal Eksperimentalnoi i Teoreticheskoi Fiziki.* 1987, roč. 93, pp. 509–518. Available also from: `https://ui.adsabs.harvard.edu/abs/1987ZhETF..93..509G`.

34. ESAREY, E.; HUBBARD, R. F.; LEEMANS, W. P.; TING, A.; SPRAN-GLE, P. Electron Injection into Plasma Wakefields by Colliding Laser Pulses. *Phys. Rev. Lett.* 1997, roč. 79, pp. 2682–2685. Available from DOI: `10.1103/PhysRevLett.79.2682`.

35. SPRANGLE, P.; ESAREY, E.; TING, A. Nonlinear theory of intense laser-plasma interactions. *Phys. Rev. Lett.* 1990, roč. 64, pp. 2011–2014. Available from DOI: `10.1103/PhysRevLett.64.2011`.

36. LU, W.; TZOUFRAS, M.; JOSHI, C.; TSUNG, F. S.; MORI, W. B.; VIEIRA, J.; FONSECA, R. A.; SILVA, L. O. Generating multi-GeV electron bunches using single stage laser wakefield acceleration in a 3D nonlinear regime. *Phys. Rev. ST Accel. Beams.* 2007, roč. 10, p. 061301. Available from DOI: `10.1103/PhysRevSTAB.10.061301`.

37. PUKHOV, A.; MEYER-TER-VEHN, J. Relativistic Magnetic Self-Channeling of Light in Near-Critical Plasma: Three-Dimensional Particle-in-Cell Simulation. *Phys. Rev. Lett.* 1996, roč. 76, pp. 3975–3978. Available from DOI: `10.1103/PhysRevLett.76.3975`.

38. REN, C.; HEMKER, R. G.; FONSECA, R. A.; DUDA, B. J.; MORI, W. B. Mutual Attraction of Laser Beams in Plasmas: Braided Light. *Phys. Rev. Lett.* 2000, roč. 85, pp. 2124–2127. Available from DOI: `10.1103/PhysRevLett.85.2124`.

39. GEDDES, C. G. R.; TOTH, Cs.; TILBORG, J. van; ESAREY, E.; SCHRO-EDER, C. B.; CARY, J.; LEEMANS, W. P. Guiding of Relativistic Laser Pulses by Preformed Plasma Channels. *Phys. Rev. Lett.* 2005, roč. 95, p. 145002. Available from DOI: `10.1103/PhysRevLett.95.145002`.

40. SHALLOO, R. J.; ARRAN, C.; CORNER, L.; HOLLOWAY, J.; JONNERBY, J.; WALCZAK, R.; MILCHBERG, H. M.; HOOKER, S. M. Hydrodynamic optical-field-ionized plasma channels. *Phys. Rev. E.* 2018, roč. 97, p. 053203. Available from DOI: `10.1103/PhysRevE.97.053203`.

41. ESAREY, E.; SPRANGLE, P.; KRALL, J.; TING, A. Self-focusing and guiding of short laser pulses in ionizing gases and plasmas. *IEEE Journal of Quantum Electronics.* 1997, roč. 33, č. 11, pp. 1879–1914. Available from DOI: `10.1109/3.641305`.

42. ESAREY, E.; SHADWICK, B. A.; SCHROEDER, C. B.; LEEMANS, W. P. Nonlinear Pump Depletion and Electron Dephasing in Laser Wakefield Accelerators. *AIP Conference Proceedings.* 2004, roč. 737, č. 1, pp. 578–584. Available from DOI: `10.1063/1.1842594`.

43. SHADWICK, B. A.; SCHROEDER, C. B.; ESAREY, E. Nonlinear laser energy depletion in laser-plasma accelerators. *Physics of Plasmas.* 2009, roč. 16, č. 5, p. 056704. Available from DOI: `10.1063/1.3124185`.

44. WENZ, J.; KARSCH, S. Physics of Laser-Wakefield Accelerators (LWFA). 2020. Available from DOI: `10.48550/ARXIV.2007.04622`.

45. LEEMANS, W. P.; NAGLER, B.; GONSALVES, A. J.; TÓTH, Cs.; NAKA-MURA, K.; GEDDES, C. G. R.; ESAREY, E.; SCHROEDER, C. B.; HOO-KER, S. M. GeV electron beams from a centimetre-scale accelerator. *Nature Physics.* 2006, roč. 2, č. 10, pp. 696–699. ISSN 1745-2481. Available from DOI: `10.1038/nphys418`.

46. GONSALVES, A. J.; NAKAMURA, K.; DANIELS, J.; BENEDETTI, C.; PIERONEK, C.; RAADT, T. C. H. de; STEINKE, S. et al. Petawatt Laser Guiding and Electron Beam Acceleration to 8 GeV in a Laser-Heated Capillary Discharge Waveguide. *Phys. Rev. Lett.* 2019, roč. 122, p. 084801. Available from DOI: `10.1103/PhysRevLett.122.084801`.

47. BULANOV, S.; NAUMOVA, N.; PEGORARO, F.; SAKAI, J. Particle injection into the wave acceleration phase due to nonlinear wake wave breaking. *Physical Review E - PHYS REV E.* 1998, roč. 58, p. 4. Available from DOI: `10.1103/PhysRevE.58.R5257`.

48. LI, F. Y.; SHENG, Z. M.; LIU, Y.; MEYER-TER-VEHN, J.; MORI, W. B.; LU, W.; ZHANG, J. Dense Attosecond Electron Sheets from Laser Wakefields Using an Up-Ramp Density Transition. *Phys. Rev. Lett.* 2013, roč. 110, p. 135002. Available from DOI: `10.1103/PhysRevLett.110.135002`.

49. BUCK, A.; WENZ, J.; XU, J.; KHRENNIKOV, K.; SCHMID, K.; HEIGOLDT, M.; MIKHAILOVA, J. M.; GEISSLER, M.; SHEN, B.; KRAUSZ, F.; KARSCH, S.; VEISZ, L. Shock-Front Injector for High-Quality Laser-Plasma Acceleration. *Phys. Rev. Lett.* 2013, roč. 110, p. 185006. Available from DOI: `10.1103/PhysRevLett.110.185006`.

50. VIEIRA, J.; MARTINS, S. F.; PATHAK, V. B.; FONSECA, R. A.; MORI, W. B.; SILVA, L. O. Magnetic Control of Particle Injection in Plasma Based Accelerators. *Phys. Rev. Lett.* 2011, roč. 106, p. 225001. Available from DOI: `10.1103/PhysRevLett.106.225001`.

51. UMSTADTER, D.; KIM, J. K.; DODD, E. Laser Injection of Ultrashort Electron Pulses into Wakefield Plasma Waves. *Phys. Rev. Lett.* 1996, roč. 76, pp. 2073–2076. Available from DOI: `10.1103/PhysRevLett.76.2073`.

52. SCHROEDER, C. B.; LEE, P. B.; WURTELE, J. S.; ESAREY, E.; LEEMANS, W. P. Generation of ultrashort electron bunches by colliding laser pulses. *Phys. Rev. E.* 1999, roč. 59, pp. 6037–6047. Available from DOI: `10.1103/PhysRevE.59.6037`.

53. YU, L.-L.; ESAREY, E.; SCHROEDER, C. B.; VAY, J.-L.; BENEDETTI, C.; GEDDES, C. G. R.; CHEN, M.; LEEMANS, W. P. Two-Color Laser-Ionization Injection. *Phys. Rev. Lett.* 2014, roč. 112, p. 125001. Available from DOI: `10.1103/PhysRevLett.112.125001`.

54. MOORE, C. I.; TING, A.; MCNAUGHT, S. J.; QIU, J.; BURRIS, H. R.; SPRANGLE, P. A Laser-Accelerator Injector Based on Laser Ionization and Ponderomotive Acceleration of Electrons. *Phys. Rev. Lett.* 1999, roč. 82, pp. 1688–1691. Available from DOI: `10.1103/PhysRevLett.82.1688`.

55. ESAREY, E.; SHADWICK, B. A.; CATRAVAS, P.; LEEMANS, W. P. Synchrotron radiation from electron beams in plasma-focusing channels. *Phys. Rev. E.* 2002, roč. 65, p. 056505. Available from DOI: `10.1103/PhysRevE.65.056505`.

56. LI, X.; NGHIEM, P. A. P.; MOSNIER, A. Toward low energy spread in plasma accelerators in quasilinear regime. *Phys. Rev. Accel. Beams.* 2018, roč. 21, p. 111301. Available from DOI: `10.1103/PhysRevAccelBeams.21.111301`.

57. ZENG, M.; CHEN, M.; SHENG, Z-M.; MORI, W. B.; ZHANG, J. Self-truncated ionization injection and consequent monoenergetic electron bunches in laser wakefield acceleration. *Physics of Plasmas*. 2014, roč. 21, č. 3, p. 030701. Available from DOI: 10.1063/1.4868404.

58. D'ARCY, R.; WESCH, S.; ASCHIKHIN, A. et al. Tunable Plasma-Based Energy Dechirper. *Phys. Rev. Lett.* 2019, roč. 122, p. 034801. Available from DOI: 10.1103/PhysRevLett.122.034801.

59. BRINKMANN, R.; DELBOS, N.; DORNMAIR, I. et al. Chirp Mitigation of Plasma-Accelerated Beams by a Modulated Plasma Density. *Phys. Rev. Lett.* 2017, roč. 118, p. 214801. Available from DOI: 10.1103/PhysRevLett.118.214801.

60. DÖPP, A.; THAURY, C.; GUILLAUME, E. et al. Energy-Chirp Compensation in a Laser Wakefield Accelerator. *Phys. Rev. Lett.* 2018, roč. 121, p. 074802. Available from DOI: 10.1103/PhysRevLett.121.074802.

61. CLAYTON, C. E.; MARSH, K. A.; DYSON, A.; EVERETT, M.; LAL, A.; LEEMANS, W. P.; WILLIAMS, R.; JOSHI, C. Ultrahigh-gradient acceleration of injected electrons by laser-excited relativistic electron plasma waves. *Phys. Rev. Lett.* 1993, roč. 70, pp. 37–40. Available from DOI: 10.1103/PhysRevLett.70.37.

62. EVERETT, M.; LAL, A.; GORDON, D.; CLAYTON, C. E.; MARSH, K. A.; JOSHI, C. Trapped electron acceleration by a laser-driven relativistic plasma wave. *Nature*. 1994, roč. 368, č. 6471, pp. 527–529. ISSN 1476-4687. Available from DOI: 10.1038/368527a0.

63. IRMAN, A.; LUTTIKHOF, M. J. H.; KHACHATRYAN, A. G.; GOOR, F. A. van; VERSCHUUR, J. W. J.; BASTIAENS, H. M. J.; BOLLER, K.-J. Design and simulation of laser wakefield acceleration with external electron bunch injection in front of the laser pulse. *Journal of Applied Physics*. 2007, roč. 102, č. 2, p. 024513. Available from DOI: 10.1063/1.2759878.

64. GORDON, D. F.; HUBBARD, R. F.; COOLEY, J. H.; HAFIZI, B.; TING, A.; SPRANGLE, P. Quasimonoenergetic electrons from unphased injection into channel guided laser wakefield accelerators. *Phys. Rev. E.* 2005, roč. 71, p. 026404. Available from DOI: 10.1103/PhysRevE.71.026404.

65. KHACHATRYAN, A. G. Trapping, compression, and acceleration of an electron beam by the laser wake wave. *Journal of Experimental and Theoretical Physics Letters*. 2001, roč. 74, č. 7, pp. 371–374. ISSN 1090-6487. Available from DOI: 10.1134/1.1427124.

66. DIJK, W. van; CORSTENS, J. M.; GEER, S. B. van der; WIEL, M. J. van der; BRUSSAARD, G. J. H. Effects of timing and stability on laser wakefield acceleration using external injection. *Phys. Rev. ST Accel. Beams*. 2009, roč. 12, p. 051304. Available from DOI: 10.1103/PhysRevSTAB.12.051304.

67. HUA, Jianfei; WU, Yipeng; LU, Wei. External injection from a Linac into a LWFA with 100% capture efficiency (Conference Presentation). *International Society for Optics and Photonics*. 2019, roč. 11037. Available from DOI: 10.1117/12.2520697.

68. WALKER, P. A.; ALESINI, P.D.; ALEXANDROVA, A. S. et al. Horizon 2020 EuPRAXIA design study. *Journal of Physics: Conference Series.* 2017, roč. 874, p. 012029. Available from DOI: `10.1088/1742-6596/874/1/012029`.

69. ROSSI, A.; ALBERTO, B.; BELLEVEGLIA, M.; CHIADRONI, E.; CIAN-CHI, A. et al. The External-Injection experiment at the SPARC$_L$ AB $facility$. *Nuclear Instruments and Methods in Physics Research Section A Accelerators Spectrometers Detectors and Associated Equipment.* 2014, roč. 740. Available from DOI: `10.1016/j.nima.2013.10.063`.

70. WEIKUM, M. K. et al. Improved Electron Beam Quality from External Injection in Laser-Driven Plasma Acceleration at SINBAD. 2017, č. 8, pp. 1707–1710. ISBN 978-3-95450-182-3. Available from DOI: `https://doi.org/10.18429/JACoW-IPAC2017-TUPIK013`.

71. ZHU, J.; ASSMANN, R. W.; DOHLUS, M.; DORDA, U.; MARCHETTI, B. Sub-fs electron bunch generation with sub-10-fs bunch arrival-time jitter via bunch slicing in a magnetic chicane. *Phys. Rev. Accel. Beams.* 2016, roč. 19, p. 054401. Available from DOI: `10.1103/PhysRevAccelBeams.19.054401`.

72. DIJK, W. van; GEER, S. B. van der; WIEL, M. J. van der; BRUSSAARD, G. J. H. Parameter study of acceleration of externally injected electrons in the linear laser wakefield regime. *Physics of Plasmas.* 2008, roč. 15, č. 9, p. 093102. Available from DOI: `10.1063/1.2977765`.

73. KALMYKOV, S. Yu.; GORBUNOV, L. M.; MORA, P.; SHVETS, G. Injection, trapping, and acceleration of electrons in a three-dimensional non-linear laser wakefield. *Physics of Plasmas.* 2006, roč. 13, č. 11, p. 113102. Available from DOI: `10.1063/1.2363172`.

74. ASSMANN, R.; GREBENYUK, J. Accelerator Physics Challenges towards a Plasma Accelerator with Usable Beam Quality. 2014, p. 4. Available from DOI: `10.18429/JACoW-IPAC2014-TUOBB01`.

75. YORK, A. G.; MILCHBERG, H. M.; PALASTRO, J. P.; ANTONSEN, T. M. Direct Acceleration of Electrons in a Corrugated Plasma Waveguide. *Phys. Rev. Lett.* 2008, roč. 100, p. 195001. Available from DOI: `10.1103/PhysRevLett.100.195001`.

76. ROSSI, Andrea R. et al. The External-Injection experiment at the SPARC_LAB facility. *Nucl. Instrum. Meth. A.* 2014, roč. 740, pp. 60–66. Available from DOI: `10.1016/j.nima.2013.10.063`.

77. GREBENYUK, J.; ASSMANN, R. W.; DORDA, U.; MARCHETTI, B. Laser-driven Acceleration with External Injection at SINBAD. 2014, č. 5, pp. 1515–1518. ISBN 978-3-95450-132-8. Available from DOI: `https://doi.org/10.18429/JACoW-IPAC2014-TUPME064`.

78. ALESINI, D.; BERTOLUCCI, S.; BIAGINI, M.; BISCARI, C. et al. An R&D program for a high brightness electron beam source at LNF. 2002, p. 3.

79. ROSSI, A. R.; PETRILLO, V.; BACCI, A.; CHIADRONI, E.; CIANCHI, A. et al. Angstrom wavelength FEL driven by 5 GeV LWFA beam with external injection. *J. Phys. Conf. Ser.* 2020, roč. 1596, č. 1, p. 012004. Available from DOI: `10.1088/1742-6596/1596/1/012004`.

80.   GORDIENKO, S.; PUKHOV, A. Scalings for ultrarelativistic laser plasmas and quasimonoenergetic electrons. *Physics of Plasmas*. 2005, roč. 12, č. 4, p. 043109. Available from DOI: `10.1063/1.1884126`.

81.   TZOUFRAS, M.; LU, W.; TSUNG, F. S.; HUANG, C.; MORI, W. B.; KATSOULEAS, T.; VIEIRA, J.; FONSECA, R. A.; SILVA, L. O. Beam loading by electrons in nonlinear plasma wakes. *Physics of Plasmas*. 2009, roč. 16, č. 5, p. 056705. Available from DOI: `10.1063/1.3118628`.

82.   QUESNEL, B.; MORA, P. Theory and simulation of the interaction of ultraintense laser pulses with electrons in vacuum. *Phys. Rev. E*. 1998, roč. 58, pp. 3719–3732. Available from DOI: `10.1103/PhysRevE.58.3719`.

83.   HSIEH, C.-T.; HUANG, C.-M.; CHANG, C.-L.; HO, Y.-C.; CHEN, Y.-S.; LIN, J.-Y.; WANG, J.; CHEN, S.-Y. Tomography of Injection and Acceleration of Monoenergetic Electrons in a Laser-Wakefield Accelerator. *Phys. Rev. Lett.* 2006, roč. 96, p. 095001. Available from DOI: `10.1103/PhysRevLett.96.095001`.

84.   FAURE, J.; RECHATIN, C.; NORLIN, A.; LIFSCHITZ, A.; GLINEC, Y.; MALKA, V. Controlled injection and acceleration of electrons in plasma wakefields by colliding laser pulses. *Nature*. 2006, roč. 444, pp. 737–9. Available from DOI: `10.1038/nature05393`.

85.   LUTTIKHOF, M.; KHACHATRYAN, A.; GOOR, F. van; BOLLER, K. J. The effect of the vacuum-plasma transition and an injection angle on electron-bunch injection into a laser wakefield. *Physics of Plasmas*. 2007, roč. 14, pp. 083101–083101. Available from DOI: `10.1063/1.2759885`.

86.   KHACHATRYAN, A. G.; LUTTIKHOF, M. J. H.; GOOR, F. van; BOLLER, K. J. Effect of the ponderomotive scattering and injection position on electron-bunch injection into a laser wakefield. *Applied Physics B*. 2007, roč. 86, pp. 41–47. Available from DOI: `10.1007/s00340-006-2469-6`.

87.   URBANUS, W. H.; DIJK, W. van; GEER, S. B. van der; BRUSSAARD, G. J. H.; WIEL, M. J. van der. Front-to-end simulations of the design of a laser wakefield accelerator with external injection. *Journal of Applied Physics*. 2006, roč. 99, č. 11, p. 114501. Available from DOI: `10.1063/1.2195382`.

88.   ASSMANN, R.; YOKOYA, K. Transverse beam dynamics in plasma-based linacs. *Nuclear Instruments and Methods in Physics Research Section A: Accelerators, Spectrometers, Detectors and Associated Equipment*. 1998, roč. 410, č. 3, pp. 544–548. ISSN 0168-9002. Available from DOI: `https://doi.org/10.1016/S0168-9002(98)00187-9`.

89.   MIGLIORATI, M.; BACCI, A.; BENEDETTI, C.; CHIADRONI, E.; FERRARIO, M.; MOSTACCI, A.; PALUMBO, L.; ROSSI, A. R.; SERAFINI, L.; ANTICI, P. Intrinsic normalized emittance growth in laser-driven electron accelerators. *Phys. Rev. ST Accel. Beams*. 2013, roč. 16, p. 011302. Available from DOI: `10.1103/PhysRevSTAB.16.011302`.

90.   MICHEL, P.; SCHROEDER, C. B.; SHADWICK, B. A.; ESAREY, E.; LEEMANS, W. P. Radiative damping and electron beam dynamics in plasma-based accelerators. *Phys. Rev. E*. 2006, roč. 74, p. 026501. Available from DOI: `10.1103/PhysRevE.74.026501`.

91. KHACHATRYAN, A. G.; IRMAN, A.; GOOR, F. A. van; BOLLER, K.-J. Femtosecond electron-bunch dynamics in laser wakefields and vacuum. *Phys. Rev. ST Accel. Beams.* 2007, roč. 10, p. 121301. Available from DOI: 10.1103/PhysRevSTAB.10.121301.

92. O'SHEA, Patrick G. Reversible and irreversible emittance growth. *Phys. Rev. E.* 1998, roč. 57, pp. 1081–1087. Available from DOI: 10.1103/PhysRevE.57.1081.

93. THAURY, C.; GUILLAUME, E.; DÖPP, A.; LEHE, R.; LIFSCHITZ, A.; TA PHUOC, K.; GAUTIER, J.; GODDET, J. P.; TAFZI, A.; FLACCO, A.; TISSANDIER, F.; SEBBAN, S.; ROUSSE, A.; MALKA, V. Demonstration of relativistic electron beam focusing by a laser-plasma lens. *Nature Communications.* 2015, roč. 6, č. 1, p. 6860. ISSN 2041-1723. Available from DOI: 10.1038/ncomms7860.

94. LINDSTROM, C. A.; ADLI, E.; BOYLE, G.; CORSINI, R.; DYSON, A. E.; FARABOLINI, W.; HOOKER, S. M.; MEISEL, M.; OSTERHOFF, J.; RÖCKEMANN, J.-H.; SCHAPER, L.; SJOBAK, K. N. Emittance Preservation in an Aberration-Free Active Plasma Lens. *Phys. Rev. Lett.* 2018, roč. 121, p. 194801. Available from DOI: 10.1103/PhysRevLett.121.194801.

95. XU, X. L.; HUA, J. F.; WU, Y. P. et al. Physics of Phase Space Matching for Staging Plasma and Traditional Accelerator Components Using Longitudinally Tailored Plasma Profiles. *Phys. Rev. Lett.* 2016, roč. 116, p. 124801. Available from DOI: 10.1103/PhysRevLett.116.124801.

96. DORNMAIR, I.; FLOETTMANN, K.; MAIER, A. R. Emittance conservation by tailored focusing profiles in a plasma accelerator. *Phys. Rev. ST Accel. Beams.* 2015, roč. 18, p. 041302. Available from DOI: 10.1103/PhysRevSTAB.18.041302.

97. CORDE, S.; THAURY, C.; LIFSCHITZ, A. et al. Observation of longitudinal and transverse self-injections in laser-plasma accelerators. *Nature Communications.* 2013, roč. 4, č. 1, p. 1501. ISSN 2041-1723. Available from DOI: 10.1038/ncomms2528.

98. HEIGOLDT, M.; POPP, A.; KHRENNIKOV, K. et al. Temporal evolution of longitudinal bunch profile in a laser wakefield accelerator. *Phys. Rev. ST Accel. Beams.* 2015, roč. 18, p. 121302. Available from DOI: 10.1103/PhysRevSTAB.18.121302.

99. DÖPP, A.; GUILLAUME, E.; THAURY, C. et al. Energy boost in laser wakefield accelerators using sharp density transitions. *Physics of Plasmas.* 2016, roč. 23, č. 5, p. 056702. Available from DOI: 10.1063/1.4946018.

100. HU, R.; LU, H.; SHOU, Y. et al. Brilliant GeV electron beam with narrow energy spread generated by a laser plasma accelerator. *Phys. Rev. Accel. Beams.* 2016, roč. 19, p. 091301. Available from DOI: 10.1103/PhysRevAccelBeams.19.091301.

101. DAWSON, J. One-Dimensional Plasma Model. *The Physics of Fluids.* 1962, roč. 5, č. 4, pp. 445–459. Available from DOI: 10.1063/1.1706638.

102. YU, S. P.; KOOYERS, G. P.; BUNEMAN, O. Time-Dependent Computer Analysis of Electron-Wave Interaction in Crossed Fields. *Journal of Applied Physics*. 1965, roč. 36, č. 8, pp. 2550–2559. Available from DOI: `10.1063/1.1714528`.

103. BIRDSALL, C. K.; LANGDON, A. B. *Plasma Physics via Computer Simulation*. CRC Press, 2018. Series in Plasma Physics. ISBN 9781482263060. Available from DOI: `https://doi.org/10.1201/9781315275048`.

104. VAHEDI, V.; SURENDRA, M. A Monte Carlo collision model for the particle-in-cell method: applications to argon and oxygen discharges. *Computer Physics Communications*. 1995, roč. 87, č. 1, pp. 179–198. ISSN 0010-4655. Available from DOI: `10.1016/0010-4655(94)00171-W`. Particle Simulation Methods.

105. GIBBON, P.; FORSTER, E. Short-pulse laser - plasma interactions. *Plasma Physics and Controlled Fusion*. 1996, roč. 38, č. 6, pp. 769–793. Available from DOI: `10.1088/0741-3335/38/6/001`.

106. TAJIMA, T. Computational Plasma Physics: With Applications To Fusion And Astrophysics. 2018. ISBN 9780429981104. Available also from: `https://books.google.sk/books?id=MmNRDwAAQBAJ`.

107. BRACKBILL, J. U. *Numerical Magnetohydrodynamics for High-Beta Plasmas*. Sv. 16. Elsevier, 1976. Methods in Computational Physics: Advances in Research and Applications. ISSN 0076-6860. Available from DOI: `10.1016/B978-0-12-460816-0.50006-3`.

108. TACCOGNA, F.; MINELLI, P. *Plasma Modeling*. Hybrid models. IOP Publishing, 2016. 2053-2563. ISBN 978-0-7503-1200-4. Available from DOI: `10.1088/978-0-7503-1200-4ch9`.

109. BIRDSALL, C. K. Particle-in-cell charged-particle simulations, plus Monte Carlo collisions with neutral atoms, PIC-MCC. *IEEE Transactions on Plasma Science*. 1991, roč. 19, č. 2, pp. 65–85. Available from DOI: `10.1109/27.106800`.

110. LAPENTA, G. Kinetic Plasma Simulation: Particle In Cell Method. 2015, pp. 76–85. Available from DOI: `10.13140/RG.2.1.3319.2801`.

111. YEE, K. Numerical solution of initial boundary value problems involving maxwell's equations in isotropic media. *IEEE Transactions on Antennas and Propagation*. 1966, roč. 14, č. 3, pp. 302–307. Available from DOI: `10.1109/TAP.1966.1138693`.

112. VILLASENOR, J.; BUNEMAN, O. Rigorous charge conservation for local electromagnetic field solvers. *Computer Physics Communications*. 1992, roč. 69, č. 2, pp. 306–316. ISSN 0010-4655. Available from DOI: `https://doi.org/10.1016/0010-4655(92)90169-Y`.

113. ALVES, E. P.; MORI, W. B.; FIUZA, F. Numerical heating in particle-in-cell simulations with Monte Carlo binary collisions. *Phys. Rev. E*. 2021, roč. 103, p. 013306. Available from DOI: `10.1103/PhysRevE.103.013306`.

114. SHADWICK, B. A.; SCHROEDER, C. B. Physical Fidelity in Particle-In-Cell Modeling of Small Debye-Length Plasmas. *AIP Conference Proceedings*. 2009, roč. 1086, č. 1, pp. 321–327. Available from DOI: `10.1063/1.3080926`.

115. ARBER, T. D.; BENNETT, K.; BRADY, C. S. et al. Contemporary particle-in-cell approach to laser-plasma modelling. *Plasma Physics and Controlled Fusion.* 2015, roč. 57, č. 11, p. 113001. Available from DOI: `10.1088/0741-3335/57/11/113001`.

116. CORMIER-MICHEL, E.; SHADWICK, B. A.; GEDDES, C. G. R.; ESAREY, E.; SCHROEDER, C. B.; LEEMANS, W. P. Unphysical kinetic effects in particle-in-cell modeling of laser wakefield accelerators. *Phys. Rev. E.* 2008, roč. 78, p. 016404. Available from DOI: `10.1103/PhysRevE.78.016404`.

117. LEHE, R.; LIFSCHITZ, A.; THAURY, C.; MALKA, V.; DAVOINE, X. Numerical growth of emittance in simulations of laser-wakefield acceleration. *Phys. Rev. ST Accel. Beams.* 2013, roč. 16, p. 021301. Available from DOI: `10.1103/PhysRevSTAB.16.021301`.

118. PLATEAU, G. R.; GEDDES, C. G. R.; THORN, D. B.; CHEN, M.; BENEDETTI, C. et al. Low-Emittance Electron Bunches from a Laser-Plasma Accelerator Measured using Single-Shot X-Ray Spectroscopy. *Phys. Rev. Lett.* 2012, roč. 109, p. 064802. Available from DOI: `10.1103/PhysRevLett.109.064802`.

119. GODFREY, B. B. Numerical Cherenkov instabilities in electromagnetic particle codes. *Journal of Computational Physics.* 1974, roč. 15, č. 4, pp. 504–521. ISSN 0021-9991. Available from DOI: `https://doi.org/10.1016/0021-9991(74)90076-X`.

120. GREENWOOD, A. D.; CARTWRIGHT, K. L.; BACA, E. A.; LUGINSLAND, J. W. On the use of FDTD to simulate systems with charged particles. 2002, roč. 3, pp. 268–271. Available from DOI: `10.1109/APS.2002.1018207`.

121. VAY, J. L.; GEDDES, C. G. R.; CORMIER-MICHEL, E.; GROTE, D. P. Numerical methods for instability mitigation in the modeling of laser wakefield accelerators in a Lorentz-boosted frame. *Journal of Computational Physics.* 2011, roč. 230, č. 15, pp. 5908–5929. ISSN 0021-9991. Available from DOI: `https://doi.org/10.1016/j.jcp.2011.04.003`.

122. GREENWOOD, A. D.; CARTWRIGHT, K. L.; LUGINSLAND, J. W.; BACA, E. A. On the elimination of numerical Cerenkov radiation in PIC simulations. *Journal of Computational Physics.* 2004, roč. 201, č. 2, pp. 665–684. ISSN 0021-9991. Available from DOI: `https://doi.org/10.1016/j.jcp.2004.06.021`.

123. PUKHOV, A. Three-dimensional electromagnetic relativistic particle-in-cell code VLPL (Virtual Laser Plasma Lab). *Journal of Plasma Physics.* 1999, roč. 61, č. 3, pp. 425–433. Available from DOI: `10.1017/S0022377899007515`.

124. NUTER, R.; TIKHONCHUK, V. Suppressing the Numerical Cherenkov Radiation in the Yee Numerical Scheme. *J. Comput. Phys.* 2016, roč. 305, č. C, pp. 66–676. ISSN 0021-9991. Available from DOI: `10.1016/j.jcp.2015.10.057`.

125. FOSTER, I.; KESSELMAN, C. (ed.). *The Grid: Blueprint for a New Computing Infrastructure.* Morgan Kaufmann Publishers Inc., 1998. ISBN 1558604758.

126. CHANDRA, R.; DAGUM, L.; MENON, R.; KOHR, D.; MAYDAN, D.; MC-DONALD, J. *Parallel Programming in OpenMP.* Elsevier Science, 2001. High performance computing. ISBN 9781558606715. Available also from: `https://books.google.com.br/books?id=18CmnqIhbhUC`.

127. QUINN, M. J. *Parallel Programming in C with MPI and OpenMP*. McGraw-Hill Higher Education, 2004. McGraw-Hill Higher Education. ISBN 978007282-2564.

128. VSB - Technical University of Ostrava. *IT4Innovations National Supercomputing Center*. 2023. Available also from: `https://www.it4i.cz/en`.

129. DAVOINE, X.; LEFEBVRE, E.; FAURE, J.; RECHATIN, C.; LIFSCHITZ, A.; MALKA, V. Simulation of quasimonoenergetic electron beams produced by colliding pulse wakefield acceleration. *Physics of Plasmas*. 2008, roč. 15, č. 11, p. 113102. Available from DOI: `10.1063/1.3008051`.

130. GOLOVANOV, A. A.; KOSTYUKOV, I. Yu. Bubble regime of plasma wakefield in 2D and 3D geometries. *Physics of Plasmas*. 2018, roč. 25, č. 10, p. 103107. Available from DOI: `10.1063/1.5047274`.

131. RECHATIN, C.; FAURE, J.; DAVOINE, J.; LUNDH, O. et al. Characterization of the beam loading effects in a laser plasma accelerator. *New Journal of Physics*. 2010, roč. 12, č. 4, p. 045023. Available from DOI: `10.1088/1367-2630/12/4/045023`.